Vertical structure of vegetated land surfaces from interferometric and polarimetric radar

Robert N. Treuhaft and Paul R. Siqueira

Jet Propulsion Laboratory, California Institute of Technology, Pasadena

Abstract. This paper describes the estimation of parameters characterizing the vertical structure of vegetated land surfaces, from combined interferometric and polarimetric radar data. Physical models expressing radar observations in terms of parameters describing vegetated land surfaces are the foundation for parameter estimation techniques. Defining a general complex cross correlation enables the unified development of models for interferometry and polarimetry, including polarimetric interferometry. Three simple physical models in this paper express this complex cross correlation in terms of vegetation parameters: (1) a randomly oriented volume, (2) a randomly oriented volume with a ground return, and (3) an oriented volume. For the first two models the parameters include vegetation height, extinction coefficient, underlying topography, and another parameter depending on ground electrical properties and roughness. For the oriented volume, additional parameters depend on the refractivity, extinction coefficients, and backscattering characteristics of waves propagating along eigenpolarizations of the vegetation volume. The above models show that the interferometric cross-correlation amplitude and the polarimetric $\{HHHH/VVVV\}$ ratio both change by about 1% per meter of vegetation height change, for experimental conditions typical of airborne and spaceborne interferometric radars. These vertical-structure sensitivities prompt a parameter estimation demonstration with two-baseline TOPSAR interferometric and zero-baseline polarimetric data from the Boreal Ecosystem-Atmosphere Study (BOREAS) Southern Study Area in Prince Albert National Park, Saskatchewan, Canada. The demonstrations show the feasibility of measuring vegetation height to better than 4.2 m, underlying topography to better than 6.5 m, and the ratio of ground-to-volume power to better than 10%, using interferometry and polarimetry, coupled with parameter-constraining assumptions, concerning the degree of surface roughness. This paper suggests that single-baseline and multibaseline fully polarimetric interferometry have the potential to obviate the need for such assumptions, thereby making parameter estimation more robust, accurate, and realistic.

1. Introduction

The vertical structure of vegetated land surfaces is an important component of the description of ecosystems. "Vertical structure" refers to the characteristics of vegetation as a function of vertical height above the ground, as well as the topographic characteristics of the underlying surface. Quantitative measurements of vegetation characteristics as a function of vertical height bear on determinations of biomass, leaf area index, and vegetation type [*Waring et al.*, 1995]. Studies of forest succession and primary production also benefit from vertical-structure information. A complex vertical structure can indicate a mature or

old-growth forest [*Franklin and Spies*, 1991], which is generally less productive than forests in early stages of maturity [*Mooney and Hobbs*, 1990]. The vertical structure of vegetation, for example, the degree of canopy closure, is also an indicator of ecosystem dynamics, including light competition and the ensuing relative populations of species [*Neilson*, 1995].

Figure 1 schematically shows the objective of this paper: the estimation of vertical-structure parameters from radar interferometric and polarimetric data. In Figure 1, letter **M** is a physical model which expresses radar observations in terms of a small number of vegetation and underlying surface parameters. As shown in the figure, **M** transforms candidate parameters into calculated observations in a loop, until the calculated observations are as close as possible to observations from radar data. The number of param-
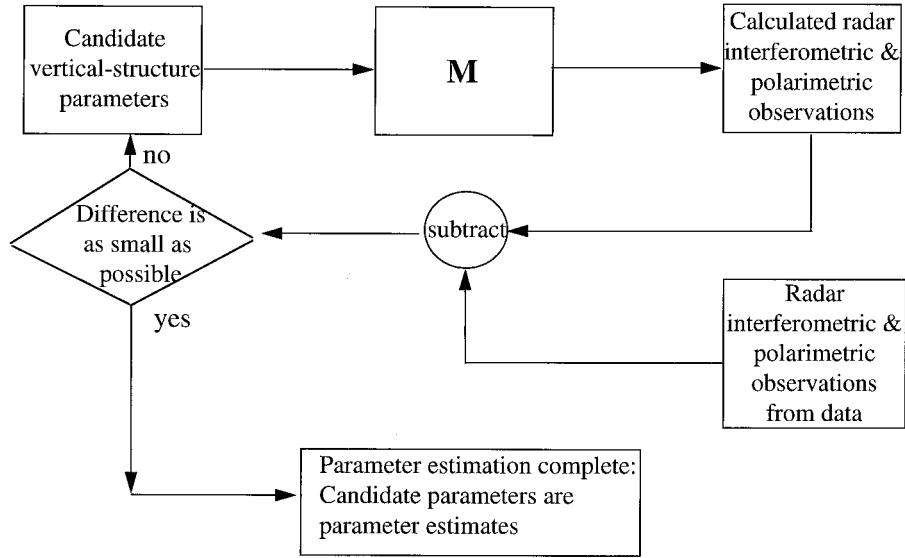
Figure 1. Schematic representation of the parameter estimation process. Candidate vegetation parameters generate model observations using the model, **M**. These are subtracted from observations, and when the magnitude of that difference is minimized, the candidate parameters become the final parameter estimates.

eters must be no greater than the number of radar observations per resolution cell (~10). The utility of relating radar observations to a small number of parameters motivates the three simple, fundamental models, **M**, described in this paper: (1) a randomly oriented volume, with negligible ground return, (2) a randomly oriented volume and a horizontal underlying surface, which induces either a specular ground-volume (called "specular") or direct-ground return (called "direct," though the ground-backscattered fields must also propagate through the randomly oriented volume before arriving at the radar receivers), and (3) an oriented volume with no contribution from the ground. These models result from a vector extension of *Treuhaft et al.* [1996] and from including ground surfaces. While these models may be oversimplified descriptions of vegetated land surfaces, their incoporation in the parameter estimation process yields reasonable results (section 3), and they serve as a foundation onto which increased model complexity can be built as needed to increase accuracy. The interferometric and polarimetric response will be related to the vertical structure of each model vegetated land surface. Before describing the qualitative signatures of vertical structure in interferometry and polarimetry, and the quantitative signatures and estimation of vertical-structure parameters, the general

radar cross-correlation observation, which will repeatedly be expressed in terms of vegetation parameters, is introduced below. This cross correlation is applicable to interferometry, polarimetry, and polarimetric interferometry. The three **M**s in this paper will express this general cross correlation in terms of parameters describing the vertical structure of vegetated land surfaces.

1.1. Interferometric, Polarimetric Cross Correlation

The complex cross correlations of signals derived from the fields returned to the radar are the primary products of interferometric and polarimetric observations. Explicitly accounting for the vector nature of those signals, the most general cross correlation, applicable to both interferometry and polarimetry, is

$$\text{cross correlation} \equiv \langle \hat{p}_1 \cdot \vec{E}_{\hat{t}_1}(\vec{R}_1)\hat{p}_2^* \cdot \vec{E}_{\hat{t}_2}^*(\vec{R}_2)\rangle, \quad (1)$$

where $\hat{p}_1$ is the receive polarization at end 1 of the baseline, located at $\vec{R}_1$, and $\vec{E}_{\hat{t}_1}(\vec{R}_1)$ is the vector signal received at $\vec{R}_1$, due to a wave transmitted at polarization $\hat{t}_1$. In (1), $\hat{p}_2$ is the receive polarization at end 2 of the baseline, while $\hat{t}_2$ is the transmit polarization, which induces the return received at end 2 of the baseline. Note that the $\hat{t}_2$ polarization can be
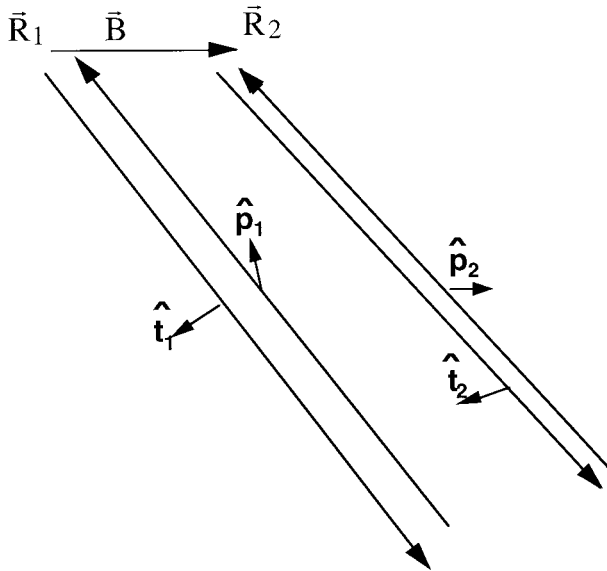
Figure 2. Interferometric signals transmitted and received at arbitrary polarizations at each end of the baseline.

transmitted from either end 1 of the baseline (single-transmit mode) or end 2 of the baseline (alternate-transmit, or "ping-pong" mode). The ensemble average angle brackets in (1) indicate average overall statistical properties of the terrain which affect the signals. In practice, multilook averaging is assumed to be equivalent to the ensemble averaging indicated in (1). Stochastic instrumental effects, such as thermal noise, which decrease the cross-correlation amplitude, are included in the ensemble average angle brackets for actual measurements but will be ignored in the modeling in this paper because they are routinely removed in data analysis.

Figure 2 schematically shows the ends of the baseline $\vec{R}_1$ and $\vec{R}_2$ with the transmit and receive polarizations. For simplicity, ping-pong mode is shown with both ends of the baseline capable of transmission

and reception. The single- and alternate-transmit configurations will be discussed in section 3. Using the standard $\hat{H}$, $\hat{V}$, and $\hat{k}$ right-handed coordinate system, with $\hat{H}$ and $\hat{V}$ the orthonormal polarization vectors and $\hat{k}$ the wave propagation direction and $\hat{H} \times \hat{V} = \hat{k}$, the vector signal at $\vec{R}_1$ in the H-V basis is

$$\vec{E}_{\hat{t}_1}(\vec{R}_1) \equiv \begin{pmatrix} \vec{E}_{\hat{t}_1}(\vec{R}_1) \cdot \hat{H} \\ \vec{E}_{\hat{t}_1}(\vec{R}_1) \cdot \hat{V} \end{pmatrix}, \qquad (2)$$

where $\vec{E}_{\hat{t}_1}(\vec{R}_1) \cdot \hat{H}$ is the signal at $\vec{R}_1$ if the receive polarization were $\hat{H}$ and the transmit were $\hat{t}_1$. In (1) the transmit and receive polarizations $\hat{t}_1$, $\hat{p}_1$, $\hat{t}_2$, and $\hat{p}_2$ can be arbitrary, linear, complex (e.g., for circular polarization) combinations of $\hat{H}$ and $\hat{V}$. The relationship between the received vector electromagnetic field and the vector signal $\vec{E}_{\hat{t}_1}(\vec{R}_1)$ involves correlation with a reference function used to compress the signal in range and azimuth [*Treuhaft et al.*, 1996] and will not be treated here.

The polarization and baseline conventions describing "interferometry" (INSAR), "polarimetry" (POLSAR), and "polarimetric interferometry" (POLINSAR) in this paper are shown in Table 1. In addition to *Treuhaft et al.* [1996], *Sarabandi* [1997] (Δk interferometry), *Wegmuller and Werner* [1997] (classification with repeat-pass interferometry), and *Hagberg et al.* [1995] (repeat-pass interferometry) have considered INSAR over vegetated surfaces. In this paper it will always be assumed that the data at each end of the baseline are simultaneously acquired. Repeat-pass interferometry, in which data acquired at different times are cross correlated, is not treated in this paper. In order to apply the approaches described here to repeat-pass interferometry, the effects of changes in vegetation position or composition between acquisition epochs must be considered. The signatures of vegetation in POLSAR have been discussed, for example, by *Cloude* [1997] and *Durden et*

Table 1. Polarization Conventions for INSAR, POLSAR, and POLINSAR in This Paper

| Data Type | Acronym | Polarization 1 | | Polarization 2 | | Baseline Length |
		Transmit	Receive	Transmit	Receive	
Interferometry	INSAR	$\hat{t}_1$	$\hat{t}_1$	$\hat{t}_1$	$\hat{t}_1$	nonzero
Polarimetry	POLSAR	$\hat{t}_1$	$\hat{p}_1$	$\hat{t}_2$	$\hat{p}_2$	zero
Polarimetric interferometry	POLINSAR	$\hat{t}_1$	$\hat{p}_1$	$\hat{t}_2$	$\hat{p}_2$	nonzero

The transmit polarization at end 1 of the baseline is $\hat{t}_1$, and $\hat{p}_1$ is the receive polarization, with similar definitions for end 2 of the baseline.
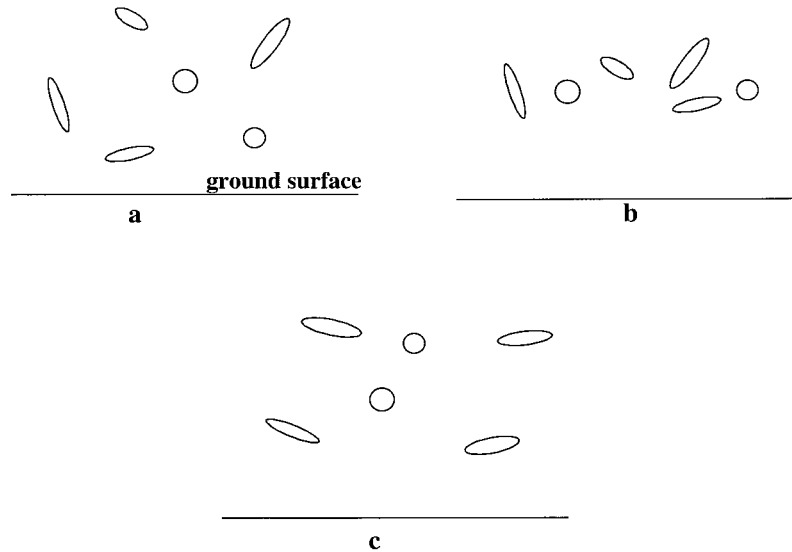
Figure 3. Scatterer geometries which produce different results in interferometry and polarimetry. Interferometry responds primarily to the difference in spatial distributions between distributed randomly oriented volume (Figure 3a) and dense randomly oriented volume (Figure 3b). Polarimetry responds primarily to the difference in orientation characteristics between the randomly oriented volume (Figure 3a or 3b) and the oriented volume (Figure 3c).

al. [1989]. *Cloude and Papathanassiou* [1998] treat POLINSAR by optimizing the amplitude of a normalized version of (1) with the choice of transmit and receive polarizations. The cross correlation in that work is formed by vectorizing the scattering matrix elements in the Pauli basis and is equivalent to (1), with the projections of the scattering matrix vectors at the ends of the baseline (called w_1 and w_2) corresponding to polarization combinations in (1). *Lin and Sarabandi* [1999] estimate vegetation properties from POLINSAR by constructing empirical relations based on fractal models.

1.2. Qualitative Signatures of Vertical Structures in Interferometric and Polarimetric Radar

By considering INSAR and POLSAR, this section provides a qualitative summary of the response of the cross correlation in (1) to the vertical structure of vegetated land surfaces. If an average value of vegetation dielectric is assumed for conceptual simplicity, the qualitative sensitivities of INSAR and POLSAR can be summarized as follows: INSAR responds primarily to the location and distribution of vegetation components and underlying surfaces, while POLSAR responds primarily to the orientation and shape of vegetation constituent scatterers. On the basis of quantitative reasoning in section 2, Figure 3 qualita-

tively illustrates the differences in the responses of interferometry and polarimetry. Figures 3a and 3b show two distributions of randomly oriented vegetation which would have very different interferometric signatures and nearly identical polarimetric signatures. As will be seen in section 2, the INSAR phase of (1) increases with mean vegetation vertical height, and therefore the phase derived from Figure 3b is greater than that for Figure 3a. The INSAR cross-correlation amplitude of Figure 3b is also greater than that of Figure 3a, because the vegetation constituents are less distributed and therefore contribute more coherently to the complex cross correlation [*Treuhaft et al.*, 1996].

In order to demonstrate the sensitivity of POLSAR to scatterer shape and orientation, Figure 3c shows a vegetation volume of scatterers with preferential orientation characteristics. This volume would have a nearly identical interferometric response to that in Figure 3a (apart from those induced by changes in extinction due to vegetation orientation) but a very different polarimetric response. The interferometric signatures of Figures 3a and 3c are nearly identical, because the distribution of scatterers is identical and the normalized version of (1) most often used in INSAR is insensitive to the change in backscattering

strength which may result from orienting the scatterers as shown in Figure 3c. On the other hand, the frequently used polarimetric ratio $\{HHHH\}/\{VVVV\}$ will depend on the projection of the average vegetation orientation onto the $\hat{H}$ and $\hat{V}$ axes (the convention $\{\hat{t}_1\hat{p}_1\hat{t}_2\hat{p}_2\}$ will be used to specify POLSAR observations, but for $\hat{H}$ or $\hat{V}$ polarizations the circumflex will be dropped); for the randomly oriented volume of Figures 3a and 3b, $\{HHHH\}/\{VVVV\} = 1$ because there is no preferred orientation for the polarization of scattered waves. Similarly, the magnitude and phase of $\{HHVV\}$ will also change as a function of orientation of the volume and the shape of the scatterers. More spherically symmetric scatterers will produce higher magnitudes of $\{HHVV\}$, while interferometric observations are comparatively insensitive to the scatterer shape or orientation.

Because of its direct sensitivity to vegetation distribution, INSAR can almost always play an important role in estimating parameters describing the vertical structure of vegetated land surfaces. If, as is often the case, the orientation of vegetation scatterers is a function of their vertical position, POLSAR can also be sensitive to vertical structure and play an additional important role in vertical-structure parameter estimation. For example, the ground surface of a forest is a horizontally oriented scatterer, at the bottom of a vegetation layer, with a polarimetric response which is very different from the more randomly oriented vegetation above it. If the vegetation height were increased, decreasing the contribution from the ground surface due to increased attenuation, POLSAR observations would respond by being less characteristic of the ground surface and more characteristic of the volume vegetation. Thus both INSAR and POLSAR observations change when vertical-structure parameters change, suggesting that combining the INSAR and POLSAR data types, including POLINSAR, may improve the accuracy of estimated parameters describing vertical structure relative to that attainable from either alone.

1.3. Approach to Quantitative Signatures and Parameter Estimation

The approach to estimating the vertical structure of vegetated land surfaces from interferometry and polarimetry in this paper is based on a quantitative description of the signatures described above. Section 2 on the quantitative modeling of the response of

interferometry and polarimetry to vertical structure treats the three model scenarios already mentioned. Although a more complicated and potentially realistic scenario arises from combining the ground return with an oriented volume, scenarios 2 and 3 are treated separately in order to understand their unique manifestations in INSAR, POLSAR, and POLINSAR. The parameters describing vegetated land surfaces, on which interferometric and polarimetric observations depend, are identified for each model scenario. Section 2 demonstrates that zero-baseline polarimetry, in the absence of a priori parameter-constraining assumptions, does not improve vertical-structure parameter estimate accuracy relative to that attained from INSAR alone, for the models considered. It also suggests, however, that POLINSAR on one or more baselines combined with zero-baseline POLSAR will yield higher parameter accuracy than INSAR alone for terrain with oriented constituents.

Section 3 first describes the sensitivity of interferometric and polarimetric observations to the vegetation parameters identified in section 2. Section 3 then describes the parameter estimation process in detail and combines INSAR and POLSAR data to demonstrate structure parameter estimate accuracy by making plausible assumptions constraining the parameters. The parameter estimation demonstration with Boreal Ecosystem-Atmosphere Study (BOREAS) data acquired with Jet Propulsion Laboratory (JPL) airborne synthetic aperture radar (AIRSAR) is intended to show the plausible potential of POLINSAR, which may provide better parameter estimate accuracies without the need for a priori assumptions. The BOREAS data demonstrate the accuracy of parameters such as tree height, underlying topography, and the ratio of ground to volume power in section 3. Section 4 contains a summary and a discussion of future data acquisition and analysis scenarios.

2. Modeling the Dependence of Interferometric and Polarimetric Observations on Vertical Structure

Parameter estimation requires physical models **M**, as in Figure 1, which express radar observations in terms of parameters describing the terrain. This section treats the quantitative response of INSAR and POLSAR by formulating three such models: (1) the randomly oriented volume, (2) the randomly oriented volume with a ground-induced return, and (3) the

oriented volume. In the sections below, for each model scenario, the most general cross correlation (equation (1)) is first expressed in terms of vegetation and surface (for the second scenario) properties. The specific INSAR and POLSAR observations which follow from the general cross correlation are then used to identify parameters describing vegetated land surfaces. Considering INSAR and POLSAR naturally suggests the application of POLINSAR. The general cross correlations derived for each model scenario below apply to POLINSAR, but the description of specific POLINSAR observations and the full set of parameters estimable from POLINSAR are beyond the scope of this paper. However, POLINSAR is repeatedly suggested when it is clear that it may enable a substantial enhancement in parameter estimation performance.

The quantitative derivation of the general cross correlation (1) augments that of *Treuhaft et al.* [1996] by introducing a ground surface and explicitly accounting for the vector nature of the fields. After deriving a general expression for the cross correlation, the specific model cross correlations will be considered in the sections below.

The signals to be cross correlated arise from a sum of signals from each scattering element, both volume and ground. The derivations of cross correlation ignore thermal noise effects. The general cross correlation can be expressed as

$$\langle \hat{p}_1 \cdot \vec{E}_{\hat{t}_1}(\vec{R}_1) \hat{p}_2^* \cdot \vec{E}_{\hat{t}_2}^*(\vec{R}_2) \rangle$$

$$= \left\langle \sum_{j=1}^{M} \hat{p}_1 \cdot \vec{E}_{\hat{t}_1}(\vec{R}_1; \vec{R}_j) \sum_{k=1}^{M} \hat{p}_2^* \cdot \vec{E}_{\hat{t}_2}^*(\vec{R}_2; \vec{R}_k) \right\rangle$$

$$= \sum_{j_v}^{M_v} \langle \hat{p}_1 \cdot \vec{E}_{\hat{t}_1}(\vec{R}_1; \vec{R}_{j_v}) \hat{p}_2^* \cdot \vec{E}_{\hat{t}_2}^*(\vec{R}_2; \vec{R}_{j_v}) \rangle$$

$$+ \sum_{j_g}^{M_g} \langle \hat{p}_1 \cdot \vec{E}_{\hat{t}_1}(\vec{R}_1; \vec{R}_{j_g}) \hat{p}_2^* \cdot \vec{E}_{\hat{t}_2}^*(\vec{R}_2; \vec{R}_{j_g}) \rangle, \qquad (3)$$

where the terms flanking the first equal sign describe the contributions of M signals, including M_v from the volume and M_g the ground. Beyond the second equal sign, (3) anticipates that only the $j = k$ terms contribute to the cross correlation; that is, a given scattering element only correlates with itself. This is because of the assumed independence of the statistical properties of the scattering elements and because

the phases of the products of elements that are separated by many wavelengths will be distributed between 0 and 2π and their contribution to the cross correlation will sum to zero (see discussion after equation (21)) [*Treuhaft et al.*, 1996]. The vector signal $\vec{E}_{\hat{t}_1}(\vec{R}_1; \vec{R}_j)$ at $\vec{R}_1$ is due to a scatterer $\vec{R}_j$. The part of (3) beyond the second equal sign separates the volume and direct-ground signals. The first sum beyond the second equal sign describes the cross correlation of signals from M_v volume scatterers, at $\vec{R}_{j_v}$, in the absence of a ground surface (see Figure 4). As will be seen below, it also describes the cross correlation due to volume scattering coupled with specular ground scattering (either ground-volume or volume-ground). The second sum in (3) describes the cross correlation due to direct ground scattering from M_g ground elements, each at $\vec{R}_{j_g}$, which will be seen below to be patches of the ground surface which are large enough so that their surface roughness patterns and dielectric constants are uncorrelated.

The angle brackets in (3) indicate ensemble averages over the spatial location of scatterers as well as their scattering characteristics. If the spatial averaging is separated out and the angle brackets are now taken to mean averaging over all other stochastic quantities (e.g., scattering amplitudes or ground dielectrics), then (3) becomes [*Treuhaft et al.*, 1996]

$$\langle \hat{p}_1 \cdot \vec{E}_{\hat{t}_1}(\vec{R}_1) \hat{p}_2^* \cdot \vec{E}_{\hat{t}_2}^*(\vec{R}_2) \rangle = \sum_{j_v=1}^{M_v} \int_{\text{volume}} d^3 R_{j_v} P_{\text{vol}}(\vec{R}_{j_v})$$

$$\cdot \langle \hat{p}_1 \cdot \vec{E}_{\hat{t}_1}(\vec{R}_1; \vec{R}_{j_v}) \hat{p}_2^* \cdot \vec{E}_{\hat{t}_2}^*(\vec{R}_2; \vec{R}_{j_v}) \rangle$$

$$+ \sum_{j_g=1}^{M_g} \int_{\text{surface}} d^2 R_{j_g} P_{\text{surf}}(\vec{R}_{j_g})$$

$$\cdot \langle \hat{p}_1 \cdot \vec{E}_{\hat{t}_1}(\vec{R}_1; \vec{R}_{j_g}) \hat{p}_2^* \cdot \vec{E}_{\hat{t}_2}^*(\vec{R}_2; \vec{R}_{j_g}) \rangle$$

$$= \int_{\text{volume}} d^3 R \, \rho_0 W_r^2 \left(\frac{\phi_1(\vec{R}_1, \vec{R})}{ik_0} - 2|\vec{R}_1 - \vec{R}_0| \right)$$

$$\cdot W_\eta^2(\eta - \eta_0) \times \langle \hat{p}_1 \cdot \vec{E}_{\hat{t}_1}(\vec{R}_1, \omega_0; \vec{R}) \hat{p}_2^* \vec{E}_{\hat{t}_2}^*(\vec{R}_2, \omega_0; \vec{R}) \rangle$$

$$(\text{V and S}) + \int_{\text{surface}} d^2 R \, \sigma_0$$

$$W_r^2 \left(\frac{\phi_1(\vec{R}_1, \vec{R})}{ik_0} - 2|\vec{R}_1 - \vec{R}_0| \right) W_\eta^2(\eta - \eta_0)$$

$$\times \langle \hat{p}_1 \cdot \vec{E}_{\hat{t}_1}(\vec{R}_1, \omega_0; \vec{R}) \hat{p}_2^* \cdot \vec{E}_{\hat{t}_2}^*(\vec{R}_2, \omega_0; \vec{R}) \rangle \, (\text{DG}), \qquad (4)$$
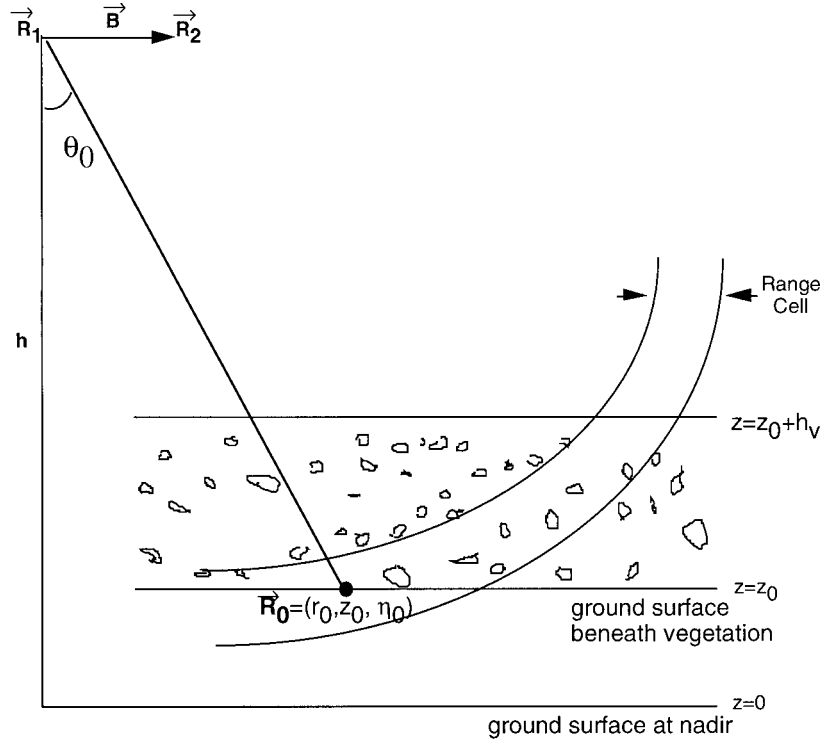
Figure 4. The interferometric scattering geometry, showing a horizontal layer of vegetation extending from $z = z_0$ to h_v, the range resolution cell, and its center at $\vec{R}_0(r_0, z_0, \eta_0)$, which is frequently used as a reference point in this paper.

where $P_{\mathrm{vol}}(\vec{R}_{j_v})$ is the probability per unit volume of a scatterer being at $\vec{R}_{j_v}$, $P_{\mathrm{surf}}(\vec{R}_{j_g})$ is the probability per unit surface area of a surface scattering element being at $\vec{R}_{j_g}$, and $k_0 = \omega_0/$the speed of light, the wavenumber at the center of the band pass. (In equations, V, S, G, and DG stand for volume, specular, ground, and direct ground, respectively.) In the last lines of (4), identical statistics have been assumed for all the volume scatterers, with spatially invariant number volume density ρ_0 [Lax, 1951]. Similarly, identical statistics have been assumed for all the surface scattering elements, with number surface density σ_0. In the last lines of (4) the signals have been expressed in terms of the Fourier component of the field at the central frequency ω_0, $\vec{E}_{\hat{t}_1}(\vec{R}_1, \omega_0; \vec{R})$, received at $\vec{R}_1$ due to a scatterer at $\vec{R}$, and range and azimuth resolution functions W_r and W_η. The term $\phi_1(\vec{R}_1, \vec{R})$ is the propagation phase of $E_{\hat{t}_1}(\vec{R}_1, \omega_0; \vec{R})$, i.e., the phase which depends on the transmitter-scatterer-receiver round-trip propagation path for the coherent wave. For example, for volume scattering, $\phi_1(\vec{R}_1, \vec{R}) = 2ik_0|\vec{R}_1 - \vec{R}|$. The argument of the range resolution

function, expressed in terms of $\phi_1(\vec{R}_1, \vec{R})$, is the length of the round-trip propagation path from $\vec{R}_1$ to the scattering element at $\vec{R}$, minus the round-trip distance between $\vec{R}_1$ and the center of the range cell at $\vec{R}_0$, shown in Figure 4. The azimuth resolution function W_η centered at azimuth angle η_0 is included for completeness but does not affect the interferometric observables because the azimuth direction (out of the paper in Figure 4) constitutes a rotation about the baseline when $\eta - \eta_0$ is small.

For each model scenario the fields in the integrands of (4) will be derived and inserted to calculate the cross correlation in the sections below. Expressing the observations typically derived from those cross correlations in terms of the vegetation parameters on which they depend constitutes formulations of **M** in the following sections. On the basis of the following subsections, Table 2 is a list of observations and the parameters on which they depend for each model scenario. Table 3 is a list of frequently used symbols in this paper with definitions, for reference. Figure 5 schematically shows all three model scenarios.

Table 2. Summary of the Observations and Parameters on Which They Depend for Each Model Scenario

Model	Observation	Parameters
Randomly oriented volume	interferometric cross correlation (V or H)	h_v, z_0, σ_x
	{$HHHH/VVVV$} ratio	none
	{$HHVV$}/$\sqrt{\{HHHH\}}\sqrt{\{VVVV\}}$	Υ_{HHVV}
Randomly oriented volume	interferometric cross correlation (V)	h_v, z_0, σ_x, $\Delta_V^{S,D}$
+ specular (S) ground	interferometric cross correlation (H)	h_v, z_0, σ_x, $\Delta_H^{S,D}$
or direct (D) ground	{$HHHH/VVVV$} ratio	h_v, σ_x, $\Delta_V^{S,D}$, $\Delta_H^{S,D}$
	{$HHVV$}/$\sqrt{\{HHHH\}}\sqrt{\{VVVV\}}$	h_v, σ_x, Υ_{HHVV}, $\Delta_{H,H,\hat{V},\hat{V}}^{S,D}$
Oriented volume	interferometric cross correlation (V or H)	h_v, z_0, σ_{x_a}, σ_{x_b}, $\chi_a - \chi_b$, $\phi_{\hat{a},\hat{H}}$, $\{\langle (\hat{p}_i \cdot \mathbf{F}_b \cdot \hat{p}_j)(\hat{p}_k \cdot \mathbf{F}_b \cdot \hat{p}_l) \rangle\}$
	{$HHHH/VVVV$} or {$HHVV$}/$\sqrt{\{HHHH\}}\sqrt{\{VVVV\}}$	same
	polarimetric interferometric cross correlations at a and b	h_v, z_0, σ_{x_a}, σ_{x_b}, $\phi_{\hat{a},\hat{H}}$

2.1. Randomly Oriented Volume

The homogeneous randomly oriented volume is the simplest model of vegetation and serves as a good starting point for considering INSAR, POLSAR, and POLINSAR. "Random orientation" means that the probability of a scatterer's being oriented in a particular direction is equal to that of its being oriented in any other.

2.1.1. Randomly oriented volume: The cross correlation.

The field needed for (4) from a randomly oriented volume scatterer at $\vec{R}$ consists of a free-space contribution represented by the multiplicative terms in (5) and the first term in the exponential, which expresses the round-trip, free-space propagation to and from the scatterer, as in Figure 5a. The other contribution to the field is represented by the second term in the exponential in (5), due to propagation into and out of the medium in the distorted Born approximation, as indicated by the rays from the scatterer at $\vec{R}$ to all other scatterers in Figure 5a. For the randomly oriented volume, using a discrete-scatterer approach [Lang, 1981], the field at end 1 of the interferometer due to a backscatterer at $\vec{R}$ is [e.g., Treuhaft et al., 1996]

$$\vec{E}_{\hat{t}_1}(\vec{R}_1, \omega_0; \vec{R}) = A^2 \mathbf{F}_{b,\vec{R}} \cdot \hat{t}_1$$

$$\cdot \exp\left[2ik_0|\vec{R}_1 - \vec{R}| + \frac{4\pi i \rho_0 \langle \hat{t} \cdot \mathbf{F}_f \cdot \hat{t} \rangle (h_v - z)}{k_0 \cos \theta_{\vec{R}}} \right],$$

$$\mathbf{F}_{b,\vec{R}} \equiv \begin{pmatrix} F_{b,\vec{R}}^{HH} & F_{b,\vec{R}}^{HV} \\ F_{b,\vec{R}}^{VH} & F_{b,\vec{R}}^{VV} \end{pmatrix}, \qquad (5)$$

where $\theta_{\vec{R}}$ is the incidence angle from $\vec{R}_1$ to $\vec{R}$, A is $1/|\vec{R}_1 - \vec{R}_0|$, and $\mathbf{F}_{b,\vec{R}}$ is the scattering amplitude matrix in the backward direction for a volume scatterer located at $\vec{R}$. It replaces the scalar backscattering amplitude f_b in the previous work. In $\mathbf{F}_{b,\vec{R}}$, $F_{b,\vec{R}}^{HH}$

is the backscattering amplitude for an incident and scattered wave of polarization $\hat{H}$. The medium propagation term in (5) induces an additional phase (via the real part of $\mathbf{F}_f$, the forward scattering matrix) and attenuation (via the imaginary part). For a randomly oriented medium, $\langle \mathbf{F}_f \rangle$ is a multiple of the identity matrix, since scattering from the $\hat{H}$ polarization to the $\hat{H}$ polarization is equivalent to its $\hat{V}$ counterpart (diagonal elements are equal); and there is no reason, on average, for a wave starting in the $\hat{H}$ polarization to rotate into the $\hat{V}$ polarization (off-diagonal elements of $\langle \mathbf{F}_f \rangle$ are zero). In (5), $\hat{t}$ is an arbitrary polarization, since the quantity $\langle \hat{t} \cdot \mathbf{F}_f \cdot \hat{t} \rangle$ is independent of polarization for a randomly oriented medium.

Inserting (5) and the analogous expression $\vec{E} \hat{t}_2(\vec{R}_2, \omega_0; \vec{R})$ for the field at end 2 of the interferometer into (4) yields the cross correlation for the randomly oriented volume. Taylor-expanding the phase of the integrands in the cross correlation around the point $\vec{R} = \vec{R}_0$ [Treuhaft et al., 1996] yields the cross correlation

$$\langle \hat{p}_1 \cdot \vec{E}_{\hat{t}_1}(\vec{R}_1) \hat{p}_2^* \cdot \vec{E}_{\hat{t}_2}^*(\vec{R}_2) \rangle = A^4 \exp\left[ik_0(r_1 - r_2)|_0 \right]$$

$$\cdot \int_0^{2\pi} W_\eta^2 \, d\eta \int_{-\infty}^{\infty} W_r^2 r_0 e^{i\alpha_r r} \, dr \cdot \int_0^{h_v} e^{i\alpha_z z} \rho_0 \langle (\hat{p}_1 \cdot \mathbf{F}_b \cdot \hat{t}_1)$$

$$\cdot (\hat{p}_2^* \cdot \mathbf{F}_b^* \cdot \hat{t}_2^*) \rangle \exp\left[\frac{-8\pi \rho_0 Im\langle \hat{t} \cdot \mathbf{F}_f \cdot \hat{t} \rangle (h_v - z)}{k_0 \cos \theta_0} \right] dz$$

$$\equiv A^4 e^{i\phi_0(z_0)} \exp\left[\frac{-2\sigma_x h_v}{\cos \theta_0} \right] \int_0^{2\pi} W_\eta^2 \, d\eta$$

$$\cdot \int_{-\infty}^{\infty} W_r^2 r_0 e^{i\alpha_r r} \, dr \cdot \rho_0 \langle (\hat{p}_1 \cdot \mathbf{F}_b \cdot \hat{t}_1)$$

$$\cdot \, (\hat{p}_2^* \cdot \mathbf{F}_b^* \cdot \hat{t}_2^*) \rangle \int_0^{h_v} e^{i\alpha_z z} \exp\left[\frac{2\sigma_x z}{\cos\theta_0}\right] dz$$

$$= A^4 e^{i\phi_0(z_0)} \exp\left[\frac{-2\sigma_x h_v}{\cos\theta_0}\right] \int_0^{2\pi} W_\eta^2 \, d\eta$$

$$\cdot \int_{-\infty}^{\infty} W_r^2 r_0 e^{i\alpha_r r} \, dr \, \rho_0 Z_v(h_v, \sigma_x, \hat{p}_1, \hat{t}_1, \hat{p}_2, \hat{t}_2), \quad (6)$$

where

$$Z_v(h_v, \sigma_x, \hat{p}_1, \hat{t}_1, \hat{p}_2, \hat{t}_2) \equiv \langle(\hat{p}_1 \cdot \mathbf{F}_b \cdot \hat{t}_1)$$

$$\cdot \, (\hat{p}_2^* \cdot \mathbf{F}_b^* \cdot \hat{t}_2^*) \rangle \int_0^{h_v} e^{i\alpha_z z} \exp\left[\frac{2\sigma_x z}{\cos\theta_0}\right] dz,$$

where $r_0 \equiv |\vec{R}_1 - \vec{R}_0|$, $r_1 \equiv |\vec{R}_1 - \vec{R}|$, and $r_2 \equiv |\vec{R}_2 - \vec{R}|$ and h_v is the height of the vegetation. The notation $|_0$ means that the differential path length to the ends of the interferometer $r_1 - r_2$ is evaluated at $\vec{R} = \vec{R}_0$, the Taylor expansion point, at the center of the range resolution element on the surface (Figure 4). Since the central range and azimuth are specified by the compression of the radar signal, z_0 completely determines $k_0(r_1 - r_2)|_0 \equiv \phi_0(z_0)$ in (6). The incidence angle at $\vec{R}_0$ is θ_0, which approximates θ_R when (5) is inserted into (4). The extinction coefficient σ_x has been defined by (6), and refractivity has been ignored (because it has negligible effect). The average product of the backscattering matrix elements indicated in Z_v is assumed to be independent of position, which is why the subscript $\vec{R}$ has been dropped. This average product is the principal difference between the vector and scalar derivation of the cross correlation, in which this term reduces to f_b^2. The argument of the range resolution function is $2|\vec{R}_1 - \vec{R}| - 2|\vec{R}_1 - \vec{R}_0|$, again, ignoring refractivity. The arguments of both the range and azimuth resolution functions have been suppressed. It will be seen that these integrations have the same value for all three model scenarios considered in this paper. In (6), α_z and α_r are the derivatives of the interferometric phase $k_0(r_1 - r_2)$ with respect to the vertical (holding the range and azimuth constant) and range (holding the vertical and azimuth constant), respectively. They are functions of the baseline vector $\vec{B}$ and are defined in Appendix B.

2.1.2. Randomly oriented volume: Observations and parameters.
This section describes interferometric and polarimetric observations and the param-

eters on which they depend and thereby specifies $\mathbf{M}$ for the randomly oriented volume. The most common observation type in interferometry is a normalized version of (6). The parameters on which this normalized cross correlation depends follow from (6), taking the limits as $\hat{t}_1, \hat{p}_1, \hat{t}_2^*, \hat{p}_2^* \rightarrow \hat{t}$, and with A_r being the normalized correlation amplitude due to the range integral in (6), which can be calculated from the hardware characteristics:

$$\frac{\langle \hat{t} \cdot \vec{E}_{\hat{t}}(\vec{R}_1)\,\hat{t}^* \cdot \vec{E}_{\hat{t}}^*(\vec{R}_2)\rangle}{\sqrt{\langle|\hat{t}\cdot\vec{E}_{\hat{t}}(\vec{R}_1)|^2\rangle}\sqrt{\langle|\hat{t}\cdot\vec{E}_{\hat{t}}(\vec{R}_2)|^2\rangle}} = \frac{2\sigma_x A_r e^{i\phi_0(z_0)}}{\cos\theta_0(e^{2\sigma_x h_v/\cos\theta_0}-1)}$$

$$\cdot \int_0^{h_v} e^{i\alpha_z z'} \exp\left[\frac{2\sigma_x z'}{\cos\theta_0}\right] dz'. \quad (7)$$

As in the work by *Treuhaft et al.* [1996], the parameters on which the interferometric cross correlation depends are (1) the vegetation height h_v, (2) the underlying topography z_0, and (3) the extinction coefficient σ_x. The interferometric sensitivity to these parameters is demonstrated by Treuhaft et al. Throughout this paper, the height parameter h_v is really the depth or thickness of the vegetation layer, while $h_v + z_0$ is the altitude of the top of the layer (see Figure 4).

The polarimetric cross correlation represents many observations, one for each combination of receive and transmit polarization. Two polarimetric observations discussed below are $\{HHHH\}/\{VVVV\}$ and the normalized cross correlation $\{HHVV\}$. Using (6), with $r_1 \rightarrow r_2$ and $\alpha_z, \alpha_r \rightarrow 0$ (polarimetry) and the fact that for randomly oriented volumes, $\langle(\hat{H} \cdot \mathbf{F}_b \cdot \hat{H})^2\rangle = \langle(\hat{V} \cdot \mathbf{F}_b \cdot \hat{V})^2\rangle$, shows that

$$\{HHHH\}/\{VVVV\} = 1, \quad (8)$$

and therefore this ratio does not depend on any of the vertical structural parameters (h_v or z_0) of the vegetation, but only on its random orientation. Another complex polarimetric observation derived from (6) is

$$\frac{\{HHVV\}}{\sqrt{\{HHHH\}}\sqrt{\{VVVV\}}}$$

$$= \frac{\langle(\hat{H} \cdot \mathbf{F}_b \cdot \hat{H})(\hat{V} \cdot \mathbf{F}_b^* \cdot \hat{V})\rangle}{\sqrt{\langle(\hat{H} \cdot \mathbf{F}_b \cdot \hat{H})^2\rangle}\sqrt{\langle(\hat{V} \cdot \mathbf{F}_b \cdot \hat{V})^2\rangle}} \equiv \Upsilon_{HHVV} \quad (9)$$

and similarly does not depend on any of the structural parameters of the vegetation but on properties of the backscattering amplitude matrix of the vegetation, as

Table 3. Definitions of the Symbols in This Paper

Symbol	Description	First Appearance
$\mathbf{M}$	model function relating radar observations to parameters describing a vegetated land surface	Figure 1
$\hat{p}_1, \hat{p}_2$	receive polarization at end 1 or 2 of the baseline or at the 1 or 2 position in the cross correlation for zero baseline	equation (1)
$\vec{E}_{\hat{t}_1}(\vec{R}_1)$	vector signal received at end 1 of baseline, located at $\vec{R}_1$, due to transmit polarization $\hat{t}_1$	equation (1)
$\hat{H} \; \hat{V}$	horizontal and vertical polarization unit vectors	equation (2)
z_0	ground surface altitude	Figure 4
$\vec{R}_0$	center of range and azimuth resolutions, at z_0	equation (4), Figure 4
ρ_0	volume number density of volume scatterers	equation (4)
σ_0	surface number density of independent surface elements	equation (4)
ω_0	microwave frequency at center of band pass	equation (4)
$\vec{E}_{\hat{t}_1}(\vec{R}_1, \omega_0; \vec{R}_v)$	vector field received at $\vec{R}_1$ due to volume scatterer at $\vec{R}_v$	equation (4)
$\vec{E}_{\hat{t}_1}(\vec{R}_1, \omega_0; \vec{R}_g)$	vector field received at $\vec{R}_1$ due to surface element at $\vec{R}_g$	equation (4)
W_r, W_η	range, azimuth resolution functions	equation (4)
k_0	microwave wavenumber at center of band pass	equation (5)
A	distance factor for spherical waves, $1/|\vec{R}_1 - \vec{R}_0|$	equation (5)
$\mathbf{F}_b, \mathbf{F}_f$	backward, forward volume scattering amplitude matrices	equation (6)
θ_0	interferometric incidence angle	equation (6)
h_v	vegetation height	equation (6)
σ_x	vegetation volume extinction coefficient	equation (6)
α_z, α_r	derivative of interferometric phase with respect to height, distance, (r, z, η) coordinate system	equation (6)
A_r	normalized cross-correlation amplitude contribution from the distribution of scatterers in range (the r integration)	equation (7)
$\phi_0(z_0)$	interferometric phase due to scatterer at $\vec{R}_0(z_0)$	equation (7)
$\{HHHH/VVVV\}$	$\hat{H}$ to $\hat{V}$, transmit and receive, polarimetric power ratio	equation (8)
Υ_{HHVV}	normalized backscattering $\{HHVV\}$ cross correlation	equation (9)
$\theta_{\vec{R}}$	incidence angle for a scatterer at $\vec{R}$	equation (5), Figure 5a
$\vec{R}_{sp1,\vec{R}}$	specular point on surface for transmission at $\vec{R}_1$ and reflection toward $\vec{R}$	equation (10), Figure 5b
$\theta_{sp1,\vec{R}}$	specular reflection incidence angle from $\vec{R}_1$ to $\vec{R}_{sp1,\vec{R}}$	equation (10), Figure 5b
$\mathbf{F}_{\vec{R}_{sp1,\vec{R}}}$	volume scattering matrix from specular ground point to $\vec{R}_1$	equation (10)
$\mathbf{R}(\theta_0)$	specular reflection matrix at angle θ_0	equation (10)
$\kappa_z, \kappa_x, \kappa_y$	derivative of interferometric phase with respect to height, x, and y, (x, y, z) coordinate system	equation (13)
$\Delta_{\hat{t}}^S$	ratio, specular/backscattering strength for $\hat{t}$	equation (14)
$\Delta_{\hat{H},\hat{H},\hat{V},\hat{V}}^S$	specular to back scattering for $HHVV$	equation (17)
W_P	surface roughness spatial power spectrum	equation (20)
$\alpha_{\hat{H},\hat{H}}, \alpha_{\hat{V},\hat{V}}$	slightly rough surface reflection coefficients	equation (21)
Δ_{t}^D	ratio direct-surface to backscattering strength, defined after equation (24)	equation (24)
$\hat{p}_a, \hat{p}_b$	eigenvectors of forward scattering matrix for oriented volumes	equation (26)
χ_a, χ_b	refractivities for each eigenvector	equation (26)
$\sigma_{x_a}, \sigma_{x_b}$	extinction coefficients for each eigenvector	equation (26)
R_{g-v}	ratio of received ground power to received volume power	equation (29)
ε_r	ground relative dielectric constant	equation (31)
Ψ	estimated direct-to-back strength parameter defined after equation (31)	equation (31)
M_I^{-1}, M_{I+P}^{-1}	interferometry and interferometry and polarimetry analysis operators	equations (30) and (32)
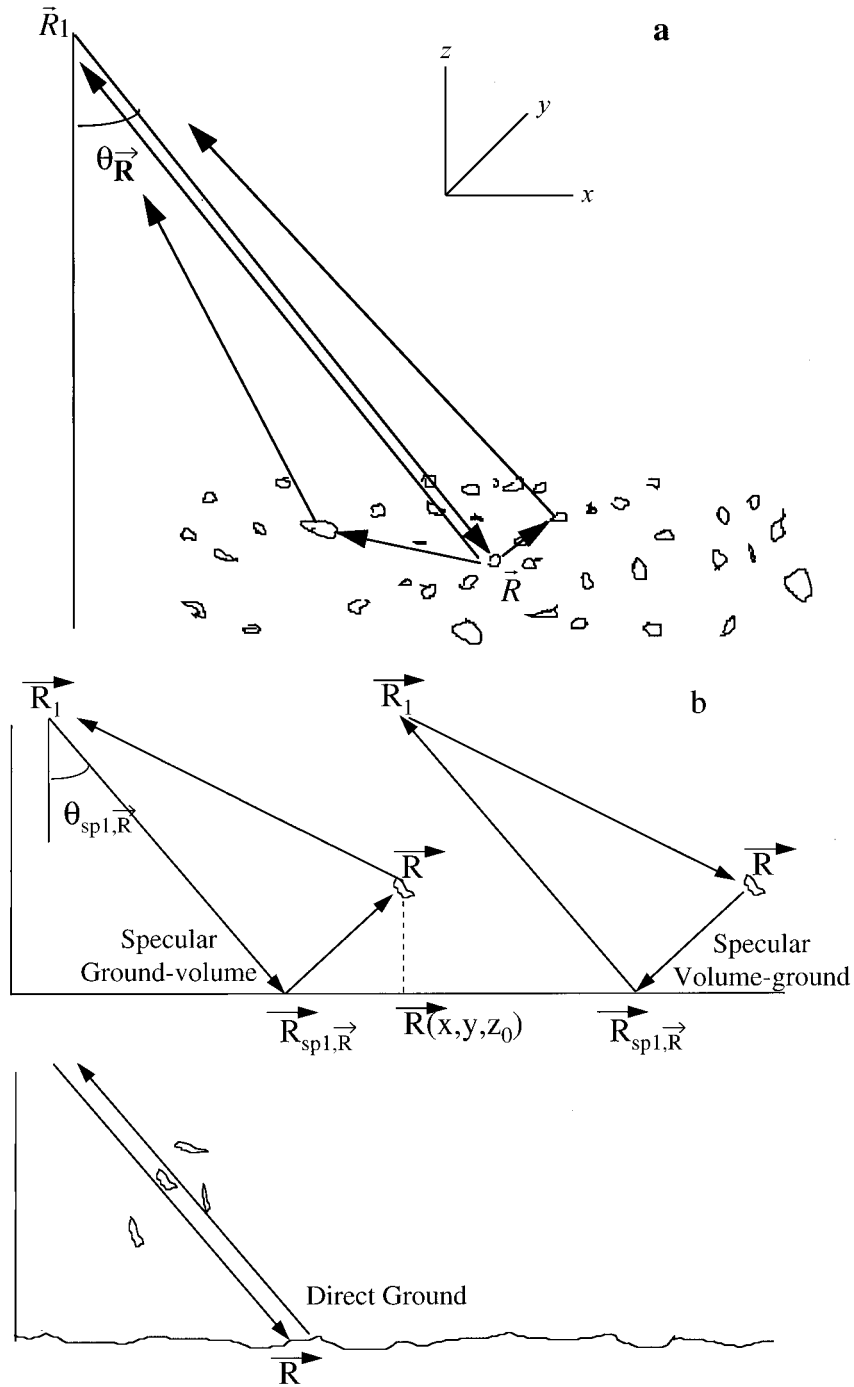
Figure 5. The three scattering mechanisms considered in this paper. (a) The randomly oriented volume scattering mechanism, showing a vegetation scatterer at $\vec{R}$ scattering directly back toward the reception point at $\vec{R}_1$ and indirectly via other scatterers in the medium. (b) The ground-volume, volume-ground, and direct-ground scattering mechanisms. The specular mechanisms involve the specular point $\vec{R}_{sp1,\vec{R}}$, while the direct mechanism involves the element of surface at $\vec{R}$. (c) The oriented volume scattering mechanism, showing two eigenpolarizations, $\hat{p}_a$ and $\hat{p}_b$. Eigenpolarization $\hat{p}_b$ propagates with higher refractivity (shorter wavelength) and higher extinction coefficient (more severe attenuation) than $\hat{p}_a$.
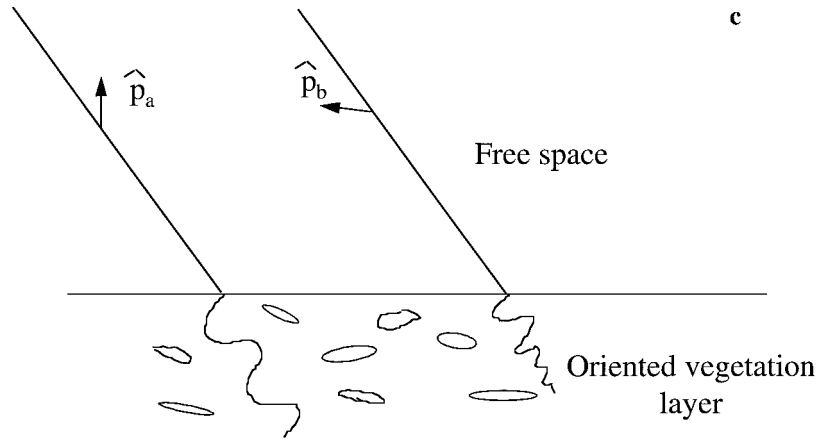
Figure 5. (continued)

indicated by the complex Υ_{HHVV} parameter, which depends on average vegetation orientation and shape.

For vertical structure information about a homogeneous, randomly oriented volume, interferometry, which depends on the vegetation height and underlying topography, is not enhanced by polarimetry, which does not. That (8) is equal to unity for randomly oriented volumes and, as will be seen later, is different from unity for either of the next two scattering scenarios suggests that the proximity of $\{HHHH\}/\{VVVV\}$ to 1 could be used as a test for the applicability of the randomly oriented volume model scenario. There are other polarimetric ratios, for example, $4\{HVHV\}/(\{HHHH\} + \{VVVV\} - 2\mathrm{Re}\{HHVV\})$ [*Nghiem et al.*, 1992], which are also equal to 1 for a randomly oriented, i.e., rotationally invariant, medium. These could also serve as tests for random orientation.

2.2. Randomly Oriented Volume With an Underlying Ground Surface

Including the cross-correlation contribution due to a ground surface incrementally increases the level of realism and complexity in modeling the dependence of interferometry and polarimetry on the vertical structure of vegetated land surfaces. When the ground contributes, adding its effect to the model increases the eventual parameter estimation accuracy and also introduces polarimetric sensitivity to vertical structure, because the ground is an oriented and therefore polarimetrically sensitive object. Two types of ground contribution will be considered: the specular return and the direct (backscattered) ground return. They are shown in Figure 5b; the two types of specular return are described in section 2.2.1. For simplicity, either the specular or direct ground mechanisms will be assumed to dominate the radar return, along with that from the randomly oriented volume. If the specular and direct ground returns are of comparable magnitude, then they will produce cross terms in the cross correlation which can be derived from an obvious extension of the treatment which follows. The cross correlation and the observations and parameters will be considered for each ground mechanism below. The specular interaction, which will be treated first, includes the ground-trunk interaction, if tree trunks are viewed as part of the volume.

2.2.1. Randomly oriented volume plus specular: Cross correlation. The specular return enters the first integral in (4) in two ways (Figure 5b): by adding a field incident on a scatterer at $\vec{R}$ due to ground reflection (at specular point $\vec{R}_{sp1,\vec{R}}$, determined by $\vec{R}_1$ and $\vec{R}$) of the incident wave from the transmitter at $\vec{R}_1$ (ground-volume) and by adding a field received at the ends of the interferometer due to ground reflection of the scattered wave from $\vec{R}$ (volume-ground). It will be assumed that the average ground slope is zero and that the statistical properties describing the ground (ground altitude and reflection coefficient) are independent of the statistical properties describing the volume.

The field to be inserted in (4) includes the volume contribution from (5) plus the ground-volume and volume-ground contributions, which are derived in Appendix A:

$$\vec{E}_{\hat{t}_1}(\vec{R}_1, \omega_0; \vec{R}) = A^2 \mathbf{F}_{b,\vec{R}} \cdot \hat{t}_1$$

$$\cdot \exp\left[2ik_0|\vec{R}_1 - \vec{R}| + \frac{4\pi i \rho_0 \langle \hat{t} \cdot \mathbf{F}_f \cdot \hat{t}\rangle(h_v - z)}{k_0 \cos \theta_{\vec{R}}}\right] \text{(V)}$$

$$+ A^2 \exp\left[ik_0\{|\vec{R}_1 - \vec{R}_{sp1,\vec{R}}| + |\vec{R} - \vec{R}_{sp1,\vec{R}}| + |\vec{R}_1\right.$$

$$\left. - \vec{R}|\} + \frac{4\pi i \rho_0 \langle \hat{t} \cdot \mathbf{F}_f \cdot \hat{t}\rangle h_v}{k_0 \cos \theta_{sp1,\vec{R}}}\right] \Gamma_{\text{rough}}$$

$$\times \mathbf{F}_{\vec{R}_{sp1,\vec{R}} \to \vec{R}_1} \langle \mathbf{R}(\theta_{sp1,\vec{R}})\rangle \cdot \hat{t}_1 \text{ (G − V)}$$

$$+ A^2 \exp\left[ik_0\{|\vec{R} - \vec{R}_1| + |\vec{R} - \vec{R}_{sp1,\vec{R}}|\right.$$

$$\left. + |\vec{R}_{sp1,\vec{R}} - \vec{R}_1|\} + \frac{4\pi i \rho_0 \langle \hat{t} \cdot \mathbf{F}_f \cdot \hat{t}\rangle h_v}{k_0 \cos \theta_{sp1,\vec{R}}}\right] \Gamma_{\text{rough}}$$

$$\times \langle \mathbf{R}(\theta_{sp1,\vec{R}})\rangle \cdot \mathbf{F}_{\vec{R}_1 \to \vec{R}_{sp1,\vec{R}}} \hat{t}_1 \text{ (V − G)}, \quad (10)$$

where the ground reflection matrix $\mathbf{R}(\theta_{sp1,\vec{R}})$ in (10), at the specular angle $\theta_{sp1,\vec{R}}$ between $\vec{R}_1$ and $\vec{R}$, is diagonal and given by

$$\mathbf{R}(\theta_{sp1,\vec{R}}) \equiv \begin{pmatrix} R_H(\theta_{sp1,\vec{R}}) & 0 \\ 0 & R_V(\theta_{sp1,\vec{R}}) \end{pmatrix}, \quad (11)$$

where R_H and R_V are the horizontal and vertical complex Fresnel reflection coefficients at $\theta_{sp1,\vec{R}}$ for H and V polarization, respectively. The reflection matrix is ensemble-averaged over ground dielectric characteristics. In (10), $\mathbf{F}_{\vec{R}_{sp1,\vec{R}} \to \vec{R}_1}$ is the scattering amplitude matrix for a volume element scattering from the ground at $\vec{R}_{sp1,\vec{R}}$ toward the receiver at $\vec{R}_1$, with the corresponding definition for $\mathbf{F}_{\vec{R}_1 \to \vec{R}_{sp1,\vec{R}}}$. For reciprocal media [*Tsang et al.*, 1985], $\mathbf{F}_{\vec{R}_{sp1,\vec{R}} \to \vec{R}_1} = \mathbf{F}_{\vec{R}_1 \to \vec{R}_{sp1,\vec{R}}}^T$.

The ground roughness term Γ_{rough} in (10) describes the loss in specular amplitude due to roughness [*Beckmann and Spizzichino*, 1963]:

$$\Gamma_{\text{rough}} \equiv \exp\left[-2k^2\sigma_H^2 \cos \theta_{sp1,\vec{R}}\right], \quad (12)$$

where σ_H is the standard deviation of the assumed Gaussian-distributed ground heights. The ground roughness term is included for completeness, but since it always multiplies the reflection coefficient, σ_H will not appear as a parameter by itself. Multifrequency interferometry and polarimetry, which are beyond the scope of this paper, could potentially be sensitive to the Γ_{rough} term by itself, as its frequency dependence could be quite different from the terms it multiplies in (10).

The phases of the ground-volume and volume-ground components of (10) are equal and contain the

total path length indicated in Figure 5b. This path length, $\vec{R}_1 \to \vec{R}_{sp1,\vec{R}} \to \vec{R}(x, y, z) \to \vec{R}_1$, is approximately equal to $2|\vec{R}_1 - \vec{R}(x, y, z_0)|$, twice the round-trip path length to a point directly below $\vec{R}$, on the ground as indicated in Appendix B (and Figure B1). The equivalence of these path lengths is used in the derivation of the cross correlation in Appendix B. Because their phases are equal, the two fields in (10) will contribute cross terms to the cross correlation calculated below. Inserting the sum of the fields in (10) into (4), along with their complex conjugates interchanging $\vec{R}_1$ and $\vec{R}_2$, therefore yields four ground terms in the interferometric cross correlation. A complete derivation is in Appendix B:

$$\langle \hat{p}_1 \cdot \vec{E}_{\hat{t}_1}(\vec{R}_1)\hat{p}_2^* \cdot \vec{E}_{\hat{t}_2}^*(\vec{R}_2)\rangle$$

$$= A^4 \exp\left[i\phi_0(z_0)\right] \exp\left[-\frac{2\sigma_x h_v}{\cos \theta_0}\right] \int_0^{2\pi} W_\eta^2 \, d\eta$$

$$\cdot \int_{-\infty}^{\infty} W_r^2 r_0 e^{i\alpha_r r} \, dr \times \rho_0 \Bigg[Z_v(h_v, \sigma_x, \hat{p}_1, \hat{t}_1, \hat{p}_2, \hat{t}_2)$$

$$\cdot \text{(V} * \text{V)} + \Gamma_{\text{rough}}^2 \langle (\hat{p}_1 \cdot \mathbf{F}_{\vec{R}_{sp1,\vec{R}} \to \vec{R}_1} \langle \mathbf{R}(\theta_0)\rangle \cdot \hat{t}_1$$

$$\cdot (\hat{p}_2^* \cdot \mathbf{F}_{\vec{R}_{sp1,\vec{R}} \to \vec{R}_1}^* \langle \mathbf{R}^*(\theta_0)\rangle \cdot \hat{t}_2^*)\rangle$$

$$\times \int_0^{h_v} dz' \, e^{i\kappa_z z'} \text{ (G − V)} * \text{(G − V)}$$

$$+ \Gamma_{\text{rough}}^2 \langle (\hat{p}_1 \cdot \mathbf{F}_{\vec{R}_{sp1,\vec{R}} \to \vec{R}_1} \langle \mathbf{R}(\theta_0)\rangle \cdot \hat{t}_1$$

$$\cdot (\hat{p}_2^* \cdot \langle \mathbf{R}^*(\theta_0)\rangle \mathbf{F}_{\vec{R}_1 \to \vec{R}_{sp1,\vec{R}}}^* \cdot \hat{t}_2^*)\rangle$$

$$\times \int_0^{h_v} dz' \, e^{-i\kappa_z z'} \text{(G − V)} * \text{(V − G)}$$

$$+ \Gamma_{\text{rough}}^2 \langle (\hat{p}_1 \cdot \langle \mathbf{R}(\theta_0)\rangle \mathbf{F}_{\vec{R}_1 \to \vec{R}_{sp1,\vec{R}}} \cdot \hat{t}_1$$

$$\cdot (\hat{p}_2^* \cdot \mathbf{F}_{\vec{R}_{sp1,\vec{R}} \to \vec{R}_1}^* \langle \mathbf{R}^*(\theta_0)\rangle \cdot \hat{t}_2^*)\rangle$$

$$\times \int_0^{h_v} dz' \, e^{i\kappa_z z'} \text{ (V − G)} * \text{(G − V)}$$

$$+ \Gamma_{\text{rough}}^2 \langle (\hat{p}_1 \cdot \langle \mathbf{R}(\theta_0)\rangle \mathbf{F}_{\vec{R}_1 \to \vec{R}_{sp1,\vec{R}}} \cdot \hat{t}_1$$

$$\cdot (\hat{p}_2^* \cdot \langle \mathbf{R}^*(\theta_0)\rangle \mathbf{F}_{\vec{R}_1 \to \vec{R}_{sp1,\vec{R}}}^* \cdot \hat{t}_2^*)\rangle$$

$$\times \int_0^{h_v} dz' \, e^{-i\kappa_z z'} \Bigg] \text{(V − G)} * \text{(V − G)} \quad (13)$$

where Z_v is as in (6), the central incidence angle, θ_0 approximates the exact specular angle for each scatterer, and the scattering amplitudes to or from the $\vec{R}_1$ direction are assumed equal to those to or from the $\vec{R}_2$ direction. In (13), κ_z is the partial derivative of interferometric phase with respect to the vertical coordinate z but holding rectangular coordinates x and y fixed. The need for holding rectangular coordinates fixed, as opposed to holding spherical coordinates fixed as in α_z, is given along with an expression for κ_z in Appendix B. The four ground terms in (13) are for the various combinations of ground-volume and volume-ground that correlate with each other. Terms involving ground-volume-ground returns (two specular reflections) have been left out because they are often small due to attenuation in the vegetation. Note that if $\hat{p}_1 = \hat{t}_1$ and $\hat{p}_2 = \hat{t}_2$ and a reciprocal volume is assumed ($\mathbf{F}_{\vec{R}_1 \to \vec{R}_{sp1,\vec{R}}} = \mathbf{F}^T_{\vec{R}_{sp1,\vec{R}} \to \vec{R}_1}$), the volume-volume term of (13) contributes a phasor with a phase somewhere in the volume, depending on extinction, while the net phase of the specular terms is $\phi_0(z_0)$, constituting a phasor from the ground. As is shown in Appendix B, if there is a transmitter at each end of the baseline (ping-pong), the effective baseline doubles, and $\kappa_z \to 0$ in (13), and the phase of the ground contributions is zero (i.e., as though generated by sources on the ground at $z = z_0$) regardless of polarization combination and reciprocity of the medium.

2.2.2. Randomly oriented volume plus specular: Observations and parameters.

Calculating the normalized interferometric cross correlation, as in (7), involves setting all polarizations to be the same in (13). With all polarizations equal to $\hat{t}$, for reciprocal media (which will be assumed), the expectation values in the last four terms of (13) become the same, and the cross correlation becomes

$$\frac{\langle \hat{t} \cdot \vec{E}_{\hat{t}}(\vec{R}_1) \hat{t}^* \cdot \vec{E}^*_{\hat{t}}(\vec{R}_2) \rangle}{\sqrt{\langle |\hat{t} \cdot \vec{E}_{\hat{t}}(\vec{R}_1)|^2 \rangle} \sqrt{\langle |\hat{t} \cdot \vec{E}_{\hat{t}}(\vec{R}_2)|^2 \rangle}}$$

$$= A_r e^{i\phi_0(z_0)} \left[\int_0^{h_v} e^{i\alpha_z z'} \exp\left[\frac{2\sigma_x z'}{\cos\theta_0} \right] dz' \right.$$

$$+ 4 \frac{\Gamma^2_{\text{rough}} \langle R_{\hat{t}}(\theta_0) \rangle^2 \langle |\hat{t} \cdot \mathbf{F}_{\vec{R}_{sp1,\vec{R}} \to \vec{R}_1} \cdot \hat{t}|^2 \rangle}{\langle |\hat{t} \cdot \mathbf{F}_b \cdot \hat{t}|^2 \rangle} h_v \frac{\sin\kappa_z h_v}{\kappa_z h_v} \right]$$

$$\times \left[\cos\theta_0 \left(\frac{e^{2\sigma_x h_v / \cos\theta_0} - 1}{2\sigma_x} \right) \right.$$

$$\left. + 4 \frac{\Gamma^2_{\text{rough}} \langle R_{\hat{t}}(\theta_0) \rangle^2 \langle |\hat{t} \cdot \mathbf{F}_{\vec{R}_{sp1,\vec{R}} \to \vec{R}_1} \cdot \hat{t}|^2 \rangle}{\langle |\hat{t} \cdot \mathbf{F}_b \cdot \hat{t}|^2 \rangle} h_v \right]^{-1} \equiv A_r e^{i\phi_0(z_0)}$$

$$\cdot \left\{ \left[\int_0^{h_v} e^{i\alpha_z z'} \exp\left[\frac{2\sigma_x z'}{\cos\theta_0} \right] dz' + 4\Delta^S_{\hat{t}} h_v \frac{\sin\kappa_z h_v}{\kappa_z h_v} \right] \right.$$

$$\left. \Big/ \left[\cos\theta_0 \left(\frac{e^{2\sigma_x h_v / \cos\theta_0} - 1}{2\sigma_x} \right) + 4\Delta^S_{\hat{t}} h_v \right] \right\}. \tag{14}$$

Again, the volume contributes a phase equivalent to one originating from a point between 0 and h_v, while the specular ground contributions come from the ground at $z = z_0$. This expression shows that four parameters completely describe the single-polarization cross correlation when the specular mechanism is added: (1) h_v, (2) z_0, (3) σ_x (as for the randomly oriented volume), and (4) $\Delta^S_{\hat{t}}$, which is defined by (14) for specular interactions and which equals $\Delta^S_{\hat{V}}$ when the interferometric transmit polarization is $\hat{V}$, as in TOPSAR. This last real parameter $\Delta^S_{\hat{V}}$ is a measure of the strength of the ground contribution relative to that of the volume contribution and is the product of the roughness loss, the reflection coefficient squared (for polarization $\hat{V}$), and the squared ratio of the specular ($\vec{R}_{sp1,\vec{R}} \to \vec{R}_1$) to backscattered amplitudes for the volume (again, for polarization $\hat{V}$). Because $\Delta^S_{\hat{V}}$ is the product of these terms, and because these terms are not sensitive to baseline, they cannot be uniquely estimated from interferometry alone.

From (13) and (14), noting that $\langle |\hat{H} \cdot \mathbf{F}_b \cdot \hat{H}|^2 \rangle = \langle |\hat{V} \cdot \mathbf{F}_b \cdot \hat{V}|^2 \rangle$ for randomly oriented volumes, the polarimetric ratio $\{HHHH\}/\{VVVV\}$ is

$$\{HHHH\}/\{VVVV\} = \left[\int_0^{h_v} \exp\left[\frac{2\sigma_x z'}{\cos\theta_0} \right] dz' + 4\Delta^S_{\hat{H}} h_v \right]$$

$$\Big/ \left[\int_0^{h_v} \exp\left[\frac{2\sigma_x z'}{\cos\theta_0} \right] dz' + 4\Delta^S_{\hat{V}} h_v \right].$$

The $\{HHHH\}/\{VVVV\}$ ratio depends on (1) h_v, (2) σ_x, (3) $\Delta^S_{\hat{V}}$, and (4) $\Delta^S_{\hat{H}}$. Comparison of (8) and (15) shows that the presence of the specular ground return sensitizes the $\{HHHH\}/\{VVVV\}$ ratio to the vertical structure parameter h_v. If the interferometric cross correlation (14) and the $\{HHHH\}/\{VVVV\}$ ratio (15) are considered together as the observation set, a total of five parameters are required (see Table 2). Because the additional parameter in (15) $\Delta^S_{\hat{H}}$ only occurs in the $\{HHHH\}/\{VVVV\}$ ratio, adding the polarimetric ratio to the interferometric observations does not improve the accuracy of structure parameters very much; it merely serves to estimate $\Delta^S_{\hat{H}}$.

However, if in addition to the normalized cross correlation in (14) with $\hat{V}$ polarization, a normalized version of $\langle \hat{H} \cdot \vec{E}_{\hat{H}}(\vec{R}_1)\hat{H} \cdot \vec{E}_{\hat{H}}^*(\vec{R}_2)\rangle$ were also measured at $\hat{H}$ (i.e., polarimetric interferometry), this additional observation would also depend on $\Delta_{\hat{H}}^S$. Using polarimetric interferometry along with the zero-baseline polarimetry in (15) would improve the estimation of structure parameters. Fully polarimetric multibaseline interferometry would further increase the observation set from which to estimate the five parameters mentioned. If assumptions are made regarding the relationship between $\Delta_{\hat{V}}^S$ and $\Delta_{\hat{H}}^S$, for example, that their ratio is equal to the ratio of the Fresnel reflection coefficients, then the parameter estimation performance changes somewhat, and introducing the $\{HHHH\}/\{VVVV\}$ ratio does improve estimation. This is equivalent to assuming that the ratios of specular to backscattering amplitudes in the $\Delta_{\hat{i}}^S$ parameters are independent of polarization. This is a detail which will not be pursued here but which might be worth exploring to improve parameter estimation when fully polarimetric interferometry is not available.

Considering another polarimetric quantity, the normalized $\{HHVV\}$ ratio, shows that the introduction of this polarimetric observation again increases the size of the parameter list on which the total interferometric and polarimetric observations depend. From (13),

$$
\frac{\{HHVV\}}{\sqrt{\{HHHH\}}\,\sqrt{\{VVVV\}}}
$$

$$
= \left[\Upsilon_{HHVV} \int_0^{h_v} \exp\left[\frac{2\sigma_x z'}{\cos\theta_0}\right] dz' + 4\Delta_{\hat{H},\hat{H},\hat{V},\hat{V}}^S\, h_v \right]
$$

$$
\Bigg/ \left\{ \sqrt{\int_0^{h_v} \exp\left[\frac{2\sigma_x z'}{\cos\theta_0}\right] dz' + 4\Delta_{\hat{H}}^S\, h_v} \right.
$$

$$
\left. \sqrt{\int_0^{h_v} \exp\left[\frac{2\sigma_x z'}{\cos\theta_0}\right] dz' + 4\Delta_{\hat{H}}^S\, h_v,} \right\} \quad (16)
$$

where Υ_{HHVV} is defined in (9) and

$$
\Delta_{\hat{H},\hat{H},\hat{V},\hat{V}}^S \equiv \langle R_{\hat{H}}(\theta_0)\rangle\langle R_{\hat{V}}^*(\theta_0)\rangle
$$

$$
[(\langle \hat{H} \cdot \mathbf{F}_{\vec{R}_{sp1,\vec{R}} \to \vec{R}_1} \cdot \hat{H}\hat{V} \cdot \mathbf{F}_{\vec{R}_{sp1,\vec{R}} \to \vec{R}_1}^*
$$

$$
\cdot \hat{V})/\sqrt{\langle|\hat{H} \cdot \mathbf{F}_b \cdot \hat{H}|^2\rangle}\,\sqrt{\langle|\hat{V} \cdot \mathbf{F}_b^* \cdot \hat{V}|^2\rangle}) \,\Gamma_{\text{rough}}^2]. \quad (17)
$$

Equations (16) and (17) show that in addition to the five parameters on which the interferometric cross correlation and $\{HHHH\}/\{VVVV\}$ ratio depend,

the normalized $\{HHVV\}$ ratio depends on (6) the real part of Υ_{HHVV}, (7) the imaginary part of Υ_{HHVV}, (8) the real part of $\Delta_{\hat{H},\hat{H},\hat{V},\hat{V}}^S$, as defined in (17), and (9) the imaginary part of $\Delta_{\hat{H},\hat{H},\hat{V},\hat{V}}^S$. These four new parameters have to do with the strengths of backscattering and specular scattering and depend on the shape and orientation of the volume scatterers and have very little to do with the vertical structure of the vegetated land surface. Once again, simply adding polarimetry adds too many new nonstructural parameters to improve estimation of structural parameters. However, with polarimetric interferometry along with the zero-baseline polarimetry above, the inclusion of the normalized $\{HHVV\}$ ratio and the consequent estimation of these new nonstructural parameters will probably improve the accuracy with which vertical structure parameters are estimated. The quantitative sensitivity of interferometry and polarimetry to ground contributions will be presented for direct-ground contributions only, in the next sections.

2.2.3. Randomly oriented volume plus direct ground: Cross correlation. This section will derive the cross correlation for the randomly oriented volume with a direct-ground contribution. The mechanism is schematically shown in the lower part of Figure 5b. The fields from the randomly oriented volume, as before, are inserted into the first integral in (4), resulting in (6), but the fields from the direct-ground return are inserted in the second integral in (4). These fields will be taken to arise from randomly distributed patches of surface, of length L on a side, where L is much greater than the distance over which surface roughness features which induce backscatter are correlated but much smaller than a range resolution cell (see Figure C1). The dielectric constant of each small patch is also assumed uncorrelated with that of any other. The field scattered from each small patch is given by the vector equivalent of the Kirchoff integral [*Jackson*, 1975; *Ishimaru*, 1978] over the patch of surface. For example, the first field needed for the second integral in (4), due to a small patch centered at $\vec{R}$, with incidence angle $\theta\vec{R}$, is given by an integral over the surface of that patch:

$$
\hat{p}_1 \cdot \vec{E}_{\hat{t}_1}(\vec{R}_1, \omega_0; \vec{R}) = \exp\left[\frac{2\pi i\rho_0\langle \hat{t} \cdot \mathbf{F}_f \cdot \hat{t}\rangle h_v}{k_0 \cos\theta_{\vec{R}}}\right]
$$

$$
\times \hat{p}_1 \cdot \left\{ \vec{\nabla} \times \int [\hat{N}' \times \vec{E}_{\hat{t}_1}(\vec{R}')]G(\vec{R}_1, \vec{R}')\, ds' \right.
$$

$$
\left. + \frac{i}{\omega_0\epsilon_0} \vec{\nabla} \times \vec{\nabla} \times \int [\hat{N}' \times \vec{H}_{\hat{t}_1}(\vec{R}')]G(\vec{R}_1, \vec{R}')\, ds' \right\}, \quad (18)
$$

where $\hat{N}'$ is a surface unit normal and $\vec{E}\,\hat{\imath}_1(\vec{R}')$ is the scattered electric field on the surface at the position $\vec{R}'$, a small distance away from $\vec{R}$, due to an incident field with polarization $\hat{\imath}_1$. In (18), $\vec{H}\,\hat{\imath}_1(\vec{R}')$ is the scattered magnetic field on the surface at $\vec{R}'$, and $G(\vec{R}_1, \vec{R}')$ is the Green's function for the reception point $\vec{R}_1$ and the integration point on the surface at $\vec{R}'$. The first term in (18) accounts for the outgoing propagation of the wave through the randomly oriented volume, and the fields inside the integrand are assumed to be generated by incident waves which have propagated through the volume.

The expression for the received field due to a surface element in (18) is completely general and could potentially be used for any degree of surface roughness. Including higher-order roughness and the associated parameters (see Appendix C) may be feasible with the more extended data set of multibaseline polarimetric interferometry in the future. Because the data set used in the demonstration which follows in section 3 was limited, and surface roughness at the site was small, the following calculation of $\vec{E}\,\hat{\imath}_1(\vec{R}')$ and $\vec{H}\,\hat{\imath}_1(\vec{R}')$, described in detail in Appendix C, assumes slightly rough surfaces ($k_0\sigma_H \ll 1$). In Appendix C the fields are shown to depend on the Fourier transform of the roughness pattern $P(\nu m, \nu n)$, with $\nu = 2\pi/L$ and m and n being integers in the Fourier sum. Inserting those fields into (18), as shown in Appendix C, yields

$$\hat{p}_1 \cdot \vec{E}\,\hat{\imath}_1(\vec{R}_1, \omega_0; \vec{R}) = \frac{ik_0}{4\pi} \frac{e^{2ik_0|\vec{R}_1 - \vec{R}|}}{|\vec{R}_1 - \vec{R}|^2} \exp\left[\frac{4\pi i\rho_0\langle \hat{t} \cdot \mathbf{F}_f \cdot \hat{t}\rangle h_v}{k_0 \cos \theta_{\vec{R}}}\right]$$

$$\cdot \int dx'\, dy' \sum_{m,n} P(\nu m, \nu n)e^{i((\nu m + 2k_0\sin\theta_{\vec{R}})x' + \nu n y')}$$

$$\cdot f_{\hat{p}_1, \hat{\imath}_1}(\nu m, \nu n), \tag{19}$$

where $f_{\hat{p}_1, \hat{\imath}_1}(\nu m, \nu n)$ is a function of the dielectric constant, scattering geometry, and $\hat{p}_1 - \hat{\imath}_1$ polarizations. The ensemble average of (19) times the complex conjugate of the analog of (19) for the field received at $\vec{R}_2$, required for insertion in (4), is (see Appendix C for missing steps)

$$\langle \hat{p}_1 \cdot \vec{E}\,\hat{\imath}_1(\vec{R}_1, \omega_0; \vec{R})\hat{p}_2^* \cdot \vec{E}_{\hat{\imath}_2}^*(\vec{R}_2, \omega_0; \vec{R})\rangle$$

$$= \frac{A^4 k_0^2 L^2}{4} W_P(-2k_0 \sin \theta_{\vec{R}}, 0)$$

$$\times \langle f_{\hat{p}_1, \hat{\imath}_1}(-2k_0 \sin \theta_{\vec{R}}, 0)f_{\hat{p}_2, \hat{\imath}_2}^*(-2k_0 \sin \theta_{\vec{R}}, 0)\rangle$$

$$\cdot e^{ik_0|\vec{R}_1 - \vec{R}| - |\vec{R}_2 - \vec{R}|} \exp\left[\frac{-2\sigma_x h_v}{\cos \theta_{\vec{R}}}\right], \tag{20}$$

where $W_P(\nu_x, \nu_y)$ is the power spectrum of the surface roughness at spatial frequencies ν_x, ν_y, as indicated in Appendix C. For slightly rough direct-surface scattering it has been shown that for backscattering [Ulaby et al., 1982; Valenzuela, 1967]

$$\langle f_{\hat{p}_1, \hat{\imath}_1}(-2k_0 \sin \theta_{\vec{R}}, 0)f_{\hat{p}_2, \hat{\imath}_2}^*(-2k_0 \sin \theta_{\vec{R}}, 0)\rangle$$

$$= 16k_0^2 \cos^4 \theta_{\vec{R}}\langle \alpha_{\hat{p}_1, \hat{\imath}_1} \alpha_{\hat{p}_2, \hat{\imath}_2}^*\rangle, \tag{21}$$

where

$$\alpha_{\hat{H},\hat{H}} = \frac{\varepsilon_r - 1}{[\cos \theta_{\vec{R}} + (\varepsilon_r - \sin^2 \theta_{\vec{R}})^{1/2}]^2}$$

$$\alpha_{\hat{V},\hat{V}} = \frac{(\varepsilon_r - 1)[\varepsilon_r \sin^2 \theta_{\vec{R}} + (\varepsilon_r - \sin^2 \theta_{\vec{R}})]}{[\varepsilon_r \cos \theta_{\vec{R}} + (\varepsilon_r - \sin^2 \theta_{\vec{R}})^{1/2}]^2}$$

$$\alpha_{\hat{H},\hat{V}} = \alpha_{\hat{V},\hat{H}} = 0 \tag{22}$$

where ε_r is the complex, relative dielectric constant of the ground.

Inserting (21) into (20) and (20) into the second integral in (4) and using (6) for the first, purely volume integral yields the cross correlation due to a randomly oriented volume over a backscattering ground surface:

$$\langle \hat{p}_1 \cdot \vec{E}\,\hat{\imath}_1(\vec{R}_1)\hat{p}_2^* \cdot \vec{E}_{\hat{\imath}_2}^*(\vec{R}_2)\rangle$$

$$= A^4 e^{i\phi_0(z_0)} \exp\left[-\frac{2\sigma_x h_v}{\cos \theta_0}\right] \int_0^{2\pi} W_\eta^2 \, d\eta$$

$$\cdot \int_{-\infty}^{\infty} W_r^2 r_0 e^{i\alpha_r r} \, dr \, [\rho_0 Z_v(h_v, \sigma_x, \hat{p}_1, \hat{\imath}_1, \hat{p}_2, \hat{\imath}_2)\, (\text{V} * \text{V})$$

$$+ 4k_0^4 \cos^4 \theta_0 W_P(-2k_0 \sin \theta_0, 0)$$

$$\cdot \langle \alpha_{\hat{p}_1, \hat{\imath}_1} \alpha_{\hat{p}_2, \hat{\imath}_2}^*\rangle]\, (\text{DG}) * (\text{DG}). \tag{23}$$

Note that in (23) the surface density of patches is taken to be $1/L^2$; that is, the surface is completely filled with patches. Also, note that the direct-ground contribution to the cross correlation in (23), like the specular ground contribution under the assumptions mentioned in section 2.2.1, contributes a phasor with phase $\phi_0(z_0)$, from the ground. This is true whether or not the surface is assumed to be slightly rough, but the polarimetric signatures in the $\alpha_{\hat{p}, \hat{\imath}}$ will change with the magnitude of surface roughness. The specular

and direct-ground mechanism each present a different parameter estimation scenario, as shown below.

2.2.4. Randomly oriented volume plus direct ground: Observations and parameters. The normalized interferometric cross correlation from (23) for the randomly oriented volume + direct-ground scenario is equivalent to the model **M** for this scenario and is given in terms of vegetation parameters by

$$
\frac{\langle \hat{t} \cdot \vec{E}_{\hat{t}}(\vec{R}_1) \, \hat{t}^* \cdot \vec{E}_{\hat{t}}^*(\vec{R}_2) \rangle}{\sqrt{\langle |\hat{t} \cdot \vec{E}_{\hat{t}}(\vec{R}_1)|^2 \rangle} \, \sqrt{\langle |\hat{t} \cdot \vec{E}_{\hat{t}}(\vec{R}_2)|^2 \rangle}} = A_r e^{i\phi_0(z_0)}
$$

$$
\cdot \left\{ \left[\int_0^{h_v} e^{i\alpha_z z'} \exp\left[\frac{2\sigma_x z'}{\cos\theta_0} \right] dz' + 4\Delta_{\hat{t}}^D \right] \right.
$$

$$
\left. \bigg/ \left[\cos\theta_0 \left(\frac{e^{2\sigma_x h_v/\cos\theta_0} - 1}{2\sigma_x} \right) + 4\Delta_{\hat{t}}^D \right] \right\}, \tag{24}
$$

where $\Delta_{\hat{t}}^D \equiv k_0^4 \cos^4\theta_0 W_P(-2k_0\sin\theta_0, 0)\langle \alpha_{\hat{t},\hat{t}} \rangle / \rho_0 \langle |\hat{t} \cdot \mathbf{F}_b \cdot \hat{t}|^2 \rangle$ represents the strength of the ground contribution, relative to the volume strength. As for the specular case, interferometry is sensitive to a volume component with a phase corresponding to a vertical height within the volume and a ground component with a phase corresponding to the ground altitude at $z = z_0$. However, comparing (24) to (14) shows that the direct-ground relative contribution containing $\Delta_{\hat{t}}^D$ in (24) does not increase with vegetation height like the analogous specular term in (14). Unlike $\Delta_{\hat{t}}^S$, it also decreases with vegetation density ρ_0. These differences simply point out that the specular return is really a volume effect, in which the waves incident on and scattered from the volume are coherently reflected by the ground. The direct-ground mechanism is a surface effect, in which the rough surface contributes new incoherently scattered returns. The four parameters describing the direct-ground return for interferometry are, for a $\hat{V}$ interferometer, (1) h_v, (2) z_0, (3) σ_x, and (4) $\Delta_{\hat{V}}^D$.

For $\{HHHH/VVVV\}$ an additional parameter (parameter 5) $\Delta_{\hat{H}}^D$ is introduced. From (23) the $\{HHHH/VVVV\}$ ratio is

$$
\{HHHH\}/\{VVVV\} = \frac{\left[\int_0^{h_v} \exp\left[\frac{2\sigma_x z'}{\cos\theta_0} \right] dz' + 4\Delta_{\hat{H}}^D \right]}{\left[\int_0^{h_v} \exp\left[\frac{2\sigma_x z'}{\cos\theta_0} \right] dz' + 4\Delta_{\hat{V}}^D \right]}. \tag{25}
$$

If the surface is assumed to be only slightly rough, then the ratio Δ_H^D/Δ_V^D is $\alpha_{\hat{H},\hat{H}}/\alpha_{\hat{V},\hat{V}}$, from (22), if the interferometry and polarimetry are done at the same incidence angle. The normalized $\{HHVV\}$ cross correlation can be derived. As in the specular case, this observation introduces the Υ_{HHVV} parameter and a $\Delta_{\hat{H},\hat{H},\hat{V},\hat{V}}^D$ parameter analogous to its specular counterpart defined in (17).

2.3. Oriented Volume

As the final model scenario, this section considers the cross correlation resulting from an oriented volume with no ground surface. Ultimately, an oriented volume with a ground surface should be considered, but this simplified treatment is intended to isolate the cross correlation and parameters which arise from each model scenario rather than from their combination. Tree trunks and branches can obviously have preferred orientation directions, and this section demonstrates the resulting interferometric and polarimetric cross-correlation signatures.

2.3.1. Oriented volume: Cross correlation. When the volume is oriented, the average forward scattering matrix $\langle \mathbf{F}_f \rangle$ in (5) is no longer a multiple of the identity matrix. As is shown in Appendix D, a wave incident on an oriented volume will propagate along two polarizations which are eigenvectors of $\langle \mathbf{F}_f \rangle$, called "eigenpolarizations" [*Tsang et al.*, 1985]. If the eigenpolarizations of a medium are $\hat{p}_a$ and $\hat{p}_b$, they will each propagate through the medium with refractivity (index of refraction -1) χ_a and χ_b and extinction σ_{x_a} and σ_{x_b}, respectively, as shown in Figure 5c. The quantity $(k_0/2\pi\rho_0)(k_0\chi_a + i\sigma_{x_a}/2)$ is the eigenvalue of the $\langle \mathbf{F}_f \rangle$ matrix corresponding to eigenvector $\hat{p}_a$. The field necessary for insertion into the first integral in (4) involves projections of the incident and received polarizations onto the eigenpolarizations and is given by (see Appendix D)

$$
\hat{p}_1 \cdot \vec{E}_{\hat{t}_1}(\vec{R}_1, \omega_0; \vec{R}) = A^2 e^{2ik_0|\vec{R}_1 - \vec{R}|} \times \sum_{i,j} (\hat{p}_1 \cdot \hat{p}_i)(\hat{t}_1 \cdot \hat{p}_j)
$$

$$
\cdot (\hat{p}_i \cdot \mathbf{F}_b \cdot \hat{p}_j) \exp\left[\frac{ik_0(\chi_i + \chi_j)(h_v - z)}{\cos\theta_{\vec{R}}} \right]
$$

$$
\cdot \exp\left[-\frac{(\sigma_{x_i} + \sigma_{x_j})(h_v - z)}{2\cos\theta_{\vec{R}}} \right]
$$

$$
\equiv A^2 e^{2ik_0|\vec{R}_1 - \vec{R}|} \vec{P}_{1,\text{eigen}}(z) \cdot \mathbf{F}_{b,\text{eigen}} \cdot \vec{T}_{1,\text{eigen}}(z),
$$

$$\vec{P}_{1,\text{eigen}} \equiv \left\langle \begin{matrix} \hat{p}_1 \cdot \hat{p}_a \exp\left[\left(\dfrac{ik_0\chi_a - \sigma_{x_a}/2}{\cos\theta_{\vec{R}}}\right)(h_v - z)\right] \\ \hat{p}_1 \cdot \hat{p}_b \exp\left[\left(\dfrac{ik_0\chi_b - \sigma_{x_b}/2}{\cos\theta_{\vec{R}}}\right)(h_v - z)\right] \end{matrix} \right\rangle, \qquad (26)$$

where the indices i and j run over the eigenpolarization labels a and b. Equation (26) expresses the field needed for (4) in matrix notation, with the vector $\vec{P}_{1,\text{eigen}}$ defined in the $(\hat{p}_a,\ \hat{p}_b)$ eigenpolarization vector basis, as opposed to the H-V basis in (2), and a similar definition for $\vec{T}_{1,\text{eigen}}$ applies. Similarly, $\mathbf{F}_{b,\text{eigen}}$ is the backscattering matrix expressed in the eigenpolarization basis, as opposed to the H-V basis in (5). Inserting (26) and its complex conjugate into the first integral in (4) yields for the cross correlation from an oriented volume:

$$\langle \hat{p}_1 \cdot \vec{E}_{\hat{t}_1}(\vec{R}_1)\hat{p}_2^* \cdot \vec{E}_{\hat{t}_2}^*(\vec{R}_2)\rangle$$

$$= A^4 e^{i\phi_0(z_0)} \int W_\eta^2\, d\eta \int W_r^2 e^{i\alpha_r r} r_0\, dr$$

$$\times \int_0^{h_v} dz\, \rho_0 e^{i\alpha_z z} \sum_{i,j,k,l} (\hat{p}_1 \cdot \hat{p}_i)(\hat{t}_1 \cdot \hat{p}_j)(\hat{p}_2^* \cdot \hat{p}_k^*)(\hat{t}_2^* \cdot \hat{p}_l^*)$$

$$\cdot \langle(\hat{p}_i \cdot \mathbf{F}_b \cdot \hat{p}_j)(\hat{p}_k^* \cdot \mathbf{F}_b^* \cdot \hat{p}_l^*)\rangle$$

$$\cdot \exp\left[\frac{ik_0(\chi_i + \chi_j - \chi_k - \chi_l)(h_v - z)}{\cos\theta_0}\right]$$

$$\cdot \exp\left[-\frac{(\sigma_{x_i} + \sigma_{x_j} + \sigma_{x_k} + \sigma_{x_l})(h_v - z)}{2\cos\theta_0}\right]$$

$$\equiv A^4 e^{i\phi_0(z_0)} \int W_\eta^2\, d\eta \int W_r^2 e^{i\alpha_r r} r_0\, dr$$

$$\times \int_0^{h_v} dz\, \rho_0 e^{i\alpha_z z} \langle(\vec{P}_{1,\text{eigen}} \cdot \mathbf{F}_{b,\text{eigen}} \cdot \vec{T}_{1,\text{eigen}})$$

$$\cdot (\vec{P}_{2,\text{eigen}}^* \cdot \mathbf{F}_{b,\text{eigen}}^* \cdot \vec{T}_{2,\text{eigen}}^*)\rangle. \qquad (27)$$

2.3.2. Oriented volume: Observations and parameters. From (27), if the polarization at which interferometry is done is not an eigenpolarization, the usual normalized cross correlation depends on many parameters. In addition to the vegetation height (h_v) and the altitude of the underlying surface (z_0), the difference in refractivity of the two eigenpolariza-

tions, $\chi_a - \chi_b$, is also a parameter, as well as the extinction coefficients for each eigenpolarization, σ_{x_a} and σ_{x_b}. In addition, the backscattering matrix averages $\langle(\hat{p}_i \cdot \mathbf{F}_b \cdot \hat{p}_j)(\hat{p}_k^* \cdot \mathbf{F}_b^* \cdot \hat{p}_l^*)\rangle$, where i, j, k, l take on the eigenpolarization indices a and b, constitute 18 new parameters (three complex parameters for each matrix in the product), if the medium is reciprocal [*Tsang et al.*, 1985]. The eigenvectors $\hat{p}_a$ and $\hat{p}_b$ can be characterized by a single parameter, $\phi_{\hat{a},\hat{H}}$, the angle between the $\hat{a}$ polarization and $\hat{H}$ (assuming that $\hat{a}$ is perpendicular to $\hat{b}$). The resulting set of 24 parameters seems prohibitive, but symmetries in the medium may reduce the number of independent parameters [*Moghaddam*, 2000], and with multibaseline polarimetric interferometry, more than 24 observations are available from which to estimate the parameters.

In the absence of symmetries, if POLINSAR is available, one approach to simplifying the parameter estimation is to use polarimetric optimization techniques to find $\phi_{\hat{a},\hat{H}}$ [*Cloude and Pottier*, 1996]. Polarimetric interferometry can then effectively be done first with $\hat{p}_1 = \hat{t}_1 = \hat{p}_2 = \hat{t}_2 = \hat{p}_a$, then with $\hat{p}_1 = \hat{p}_b$, $\hat{t}_1 = \hat{p}_a$, $\hat{p}_2 = \hat{p}_b$, $\hat{t}_2 = \hat{p}_a$, and finally with $\hat{p}_1 = \hat{t}_1 = \hat{p}_2 = \hat{t}_2 = \hat{p}_b$. The three cross correlations at the eigenpolarizations, coupled with the zero-baseline polarimetry used in optimization, depend on the parameters: (1) h_v, (2) z_0, (3) σ_{x_a}, (4) σ_{x_b}, and (5) $\phi_{\hat{a},\hat{H}}$, a tractable parameter set which could be estimated with single-baseline PO-LINSAR [*Treuhaft and Cloude*, 1999].

3. Parameter Estimate Accuracy

This section addresses the accuracy of the vegetation and surface parameters enumerated in the previous section. The estimation of parameters can be viewed schematically as [*Hamilton*, 1964]

$$\begin{pmatrix} \text{param}_1 \\ \text{param}_2 \\ \vdots \end{pmatrix} = \mathbf{M}^{-1} \begin{pmatrix} \text{obs}_1 \\ \text{obs}_2 \\ \vdots \end{pmatrix}, \qquad (28)$$

where the left-hand column vector represents the vegetation and surface parameters to be estimated and the right-hand column vector represents the observations available, such as those in the middle column of Table 2. In (28), $\mathbf{M}^{-1}$ is an operator which gives the optimal parameter estimates (as defined below in equation (33)) as a function of the observations and is the equivalent of the process described in Figure 1. (The nonlinear estimation operator $\mathbf{M}^{-1}$ is

strictly not the inverse of the physical model **M**, but is represented by Figure 1, in which **M** is used.) That process uses **M** based on equations such as (7), (9), (14), (15), (16), (24), (25), and (27). The error in the parameter vector arises from an assessment of the errors in the observations and in **M**. In section 3.1 below, the sensitivity of the observations to parameters, related by models derived in this paper, is first explored. In general, the more sensitive an observation is to a parameter, the more accurate the parameter estimate is. In section 3.2, parameter estimate results from the BOREAS project demonstrate the feasibility of interferometry + polarimetry for determining vegetation and surface parameters. This section will focus on vegetation height h_v, the surface topography z_0, and the ratio of ground to volume power, R_{g-v}, which is a function of parameters to be shown below. It will be shown that interferometry + polarimetry and ultimately polarimetric interferometry have the potential of determining h_v to 4.2 m, z_0 to 6.5 m, and R_{g-v} to 10%, for data types and accuracies typical of TOPSAR in 1995, the epoch of the data demonstration. All of these accuracies should improve with instrumentation currently becoming available.

3.1. Observation Sensitivity to Parameters

In order to understand parameter estimate accuracy as a function of the array of observations available, the sensitivities of the interferometric cross-correlation amplitude and the {$HHHH/VVVV$} ratio to vegetation height are considered in Figure 6a, for a randomly oriented volume with a direct-ground return. The direct-ground mechanism discussed in the second model scenario was chosen because it appears to dominate the C-band data shown in the section 3.2. The sensitivity of a randomly oriented volume only is shown in two of the curves in Figure 6a, using (7) to determine the normalized cross-correlation amplitude and (8) to show the {$HHHH/VVVV$} ratio. Equations (24) and (25) determine the "volume + ground" curves in Figure 6a. In order to determine the cross-correlation amplitude and the {$HHHH/VVVV$} ratio, in addition to the vegetation height h_v on the abscissa, the extinction coefficient σ_x and the ratios Δ_V^D and Δ_H^D must be specified. The extinction coefficient was taken to be 0.3 dB/m, and Δ_V^D was taken to be equal to $10\alpha_{\hat{V},\hat{V}}^2$, with $\alpha_{\hat{V},\hat{V}}$ as in (22) at 35° incidence, with a similar relationship for Δ_H^D. The values of Δ_V^D and Δ_H^D were chosen to represent slightly rough surface scattering, with the

ratio of ground to volume received power, R_{g-v}, at $\hat{V}$ polarization about 10% for $h_v = 20$ m, as is typical of many forest types [*Moghaddam and Saatchi*, 1995; *Freeman and Durden*, 1998]. From (24) this ratio is

$$R_{g-v} = \frac{4\gamma\Delta_{\hat{V}}^D}{e^{\gamma h_v} - 1}, \tag{29}$$

where $\gamma \equiv 2\sigma_x/\cos\theta_0$. The baseline used for Figure 6a was 5 m, at a radar altitude of 7980 m. It can be seen that for the volume + ground curve, a change in vegetation height of 10 m produces about a 10% change in the cross-correlation amplitude between 10- and 20-m heights and a smaller change for higher heights. Therefore, if the interferometric cross-correlation amplitude could be measured with ~1% accuracy, few-meter vegetation height determinations should result. Figure 6a also implies that the correlation amplitude is more sensitive to vegetation height changes when there is some contribution from the ground, and therefore the presence of a ground return can improve the accuracy of the height estimate. The change in {$HHHH/VVVV$} ratio for a 10-m change in vegetation height is between 5% and 15%, also showing that a few-percent determination of {$HHHH/VVVV$} ratio could help to determine vegetation height to a few meters. Again, because the {$HHHH/VVVV$} ratio is only sensitive to vegetation height if the ground return contributes (for a randomly oriented volume), including polarimetry in the presence of a ground return can (with parameter-constraining assumptions as mentioned below) enable improved vegetation height estimation.

Figure 6b is an example of the sensitivity of polarimetry to an oriented volume. A calculation of the oriented-volume cross correlation from (27) assumed small dipoles with preferred orientations, which led to expressions for the extinction coefficients and refractivities and the $\langle(\hat{p}_i \cdot \mathbf{F}_b \cdot \hat{p}_j)(\hat{p}_k^* \cdot \mathbf{F}_b^* \cdot \hat{p}_l^*)\rangle$ backscattering terms needed in (27). Dipoles were assumed to be oriented with equal probability with polar angle between 5° and 95° and with uniform azimuthal angle (between 0° and 360°). The restricted polar-angle range generates the orientation characteristics of the volume. The azimuthal symmetry causes the average forward scattering matrix of the medium, $\langle\mathbf{F}_f\rangle$, to be diagonal, and there is therefore no rotation of an $\hat{H}$ or $\hat{V}$ polarization vector as it propagates through the oriented medium. If the extinction coefficient at $\hat{V}$ polarization of the oriented volume is again taken to be 0.3 dB/m, as in Figure 6a,
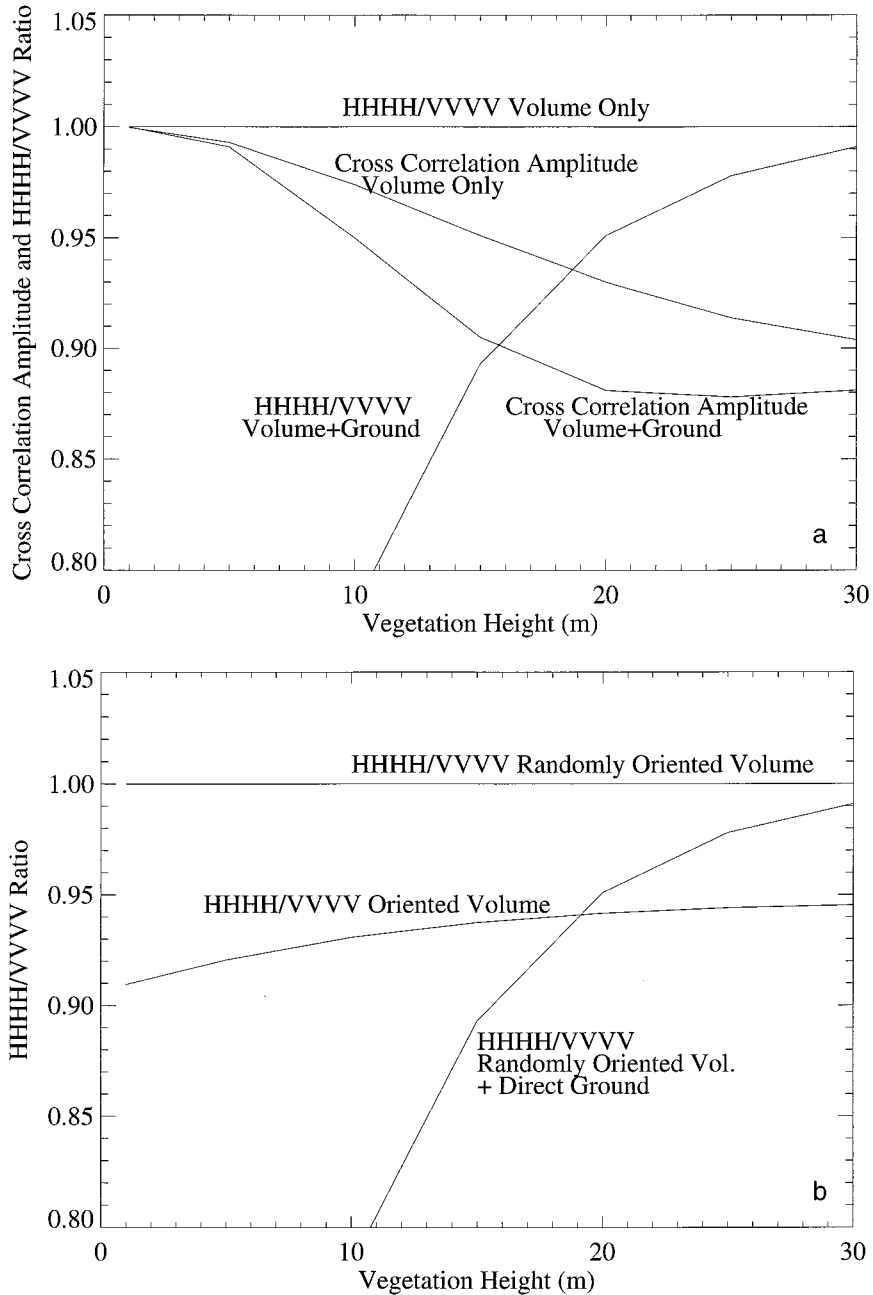
Figure 6.   (a) The calculated interferometric cross-correlation amplitude and polarimetric {*HHHH/ VVVV*} ratio as a function of vegetation height, for volume-only and volume + ground radar returns. The volume is assumed randomly oriented in both cases, with an extinction coefficient of 0.3 dB/m. The baseline used in the calculation was 5 m, the radar altitude was 7980 m, and the wavelength was 5.6 cm. The strength of the ground contribution was such that the ratio of ground to volume power was about 10% for a 20-m vegetation height. (b) The calculated {*HHHH/VVVV*} ratio as a function of vegetation height for an oriented vegetation volume of dipoles, constrained to have polar angles between 5° and 95°, with azimuthal symmetry. The {*HHHH/VVVV*} ratios for the randomly oriented and ground + volume mechanisms are shown for reference.

Table 4. Cross-Correlation Amplitudes (Corrected for Noise Contributions) and Phases, the $\{HHHH/VVVV\}$ Ratios, and Incidence Angles From the BOREAS Data

Stand	2.5-m Amplitude	2.5-m Phase, deg	5-m Amplitude	5-m Phase, deg	$HHHH/VVVV$ Ratio	θ_0, deg	θ_p, deg
1	0.959 (0.003)	40.5 (2.9)	0.844 (0.006)	62.9 (5.1)	0.898 (0.016)	29.3	56.6
2	0.921 (0.007)	57.8 (1.1)	0.724 (0.024)	104.3 (5.9)	0.916 (0.022)	28.0	59.6
3	0.977 (0.004)	45.1 (5.2)	0.913 (0.010)	80.0 (8.4)	0.926 (0.022)	32.7	56.6
4	0.974 (0.001)	13.7 (0.5)	0.895 (0.005)	22.7 (0.9)	0.914 (0.032)	33.4	54.4
5	0.974 (0.002)	8.9 (0.4)	0.903 (0.007)	21.7 (1.5)	0.960 (0.027)	37.1	52.5
6	1.001 (0.001)	0 (0.3)	1.001 (0.002)	0 (0.98)	1.270 (0.024)	36.5	53.7
7	0.999 (0.002)	0.2 (1.9)	1.003 (0.005)	2.7 (3.3)	0.917 (0.025)	39.8	52.5
8	0.999 (0.001)	7.2 (0.8)	0.987 (0.001)	16.9 (2.1)	0.985 (0.032)	41.5	51.3
9	0.997 (0.002)	−23.5 (0.3)	0.978 (0.005)	−58.4 (0.6)	0.985 (0.037)	28.4	56.0
10	0.987 (0.003)	37.5 (0.9)	0.945 (0.010)	82.8 (1.4)	0.991 (0.021)	41.5	47.4

Stand numbers correspond to Figure 7. Observation standard deviations are in parentheses.

the interferometric cross correlation for the oriented volume is exactly the same as the "volume-only" cross correlation for the randomly oriented volume. That is, orienting a volume with azimuthal symmetry (eigenpolarizations are $\hat{H}$ and $\hat{V}$) does not change the interferometric cross-correlation amplitude at $\hat{V}$ or $\hat{H}$, if the extinction coefficient is not changed. The $\{HHHH/VVVV\}$ ratio, however, does change. Figure 6b shows that the $\{HHHH/VVVV\}$ signatures due to an oriented volume can be of the same order as those due to a randomly oriented volume and a ground surface. Parameters estimated by assuming a randomly oriented volume plus a ground surface may therefore be in error if the volume is actually oriented. Ideally, both an oriented volume and a ground surface would be included in the model **M**, but the number of parameters describing such a model would require fully polarimetric interferometry at a few baselines.

3.2. Parameter Estimate Accuracies From Data

The data demonstration in this section shows the plausibility of combining interferometry and polarimetry based on the simple parameter dependencies in the text and summarized in Table 2. Because the data in the demonstration which follows are limited and consist of two interferometric baselines at $\hat{V}$ and zero-baseline polarimetry, only the randomly oriented volume + direct-ground surface will be included in **M** used in the parameter estimation. Volume orientation effects will be regarded as a possible source of error. The direct-ground mechanism from a slightly rough surface will be assumed below because for all but one of the 10 stands observed, the $\{HHHH/VVVV\}$ ratio is less than 1. From (15), (22), and (25) it follows that because $R_{\hat{H}}(\theta_0) > R_{\hat{V}}(\theta_0)$

(specular) and because $\alpha_{\hat{H},\hat{H}} < \alpha_{\hat{V},\hat{V}}$ (direct), the sign of $\{HHHH/VVVV\} - 1$ is a reasonable discriminator between specular (positive) or direct (negative) contributions. With the expanded data set of multibaseline polarimetric interferometry, both ground mechanisms could be considered and the slightly rough assumption would not be necessary, but that is beyond the scope of the present demonstration.

The interferometric data were collected at the BOREAS Southern Study Area in Prince Albert National Park, Saskatchewan, Canada, in July 1995. The part of the site used is reasonably flat, obviating the need for estimating ground slope parameters not treated in any of the model scenarios described. The data were taken with TOPSAR [*Zebker et al.*, 1992] (interferometry at $\hat{V}$ polarization) at C band (wavelength = 5.6 cm) in "ping-pong" mode. Ping-pong refers to the data acquisition mode in which signals are alternately transmitted from each end of the baseline. By following the derivation of the cross correlation of *Treuhaft et al.* [1996], it can be shown that ping-pong acquisition, for a direct-ground + randomly oriented volume mechanism, results in an effective doubling of the usual 2.5-m TOPSAR baseline, yielding the additional 5-m baseline used in this analysis. The interferometric data were taken at an aircraft altitude of approximately 7.5 km. The $\{HHHH/VVVV\}$ ratios were collected with AIRSAR (zero-baseline polarimetry) in July 1994 over the same area.

The interferometric cross-correlation amplitudes and phases, as well as the $\{HHHH/VVVV\}$ ratios, incidence angles, field-measured height, and radar-estimated height, are given in Table 4. The cross-correlation amplitudes in Table 4 have been cor-

rected for thermal noise effects by dividing the raw amplitude by that for the cross correlation of signals transmitted at end 1 and received at end 2, with those transmitted at end 2 and end 1. This "zero-baseline" interferometric cross correlation is dominated by the thermal noise contribution. The range correlation effects, represented by A_r throughout section 2, have been removed by modeling the finite bandwidth chirp structure, which typically induces a 1–3% reduction in correlation [*Treuhaft et al.*, 1996]. That some of the cross-correlation amplitudes are slightly greater than 1.0 is a lower-bound indication of the error in the above two amplitude corrections. Coincident interferometric and polarimetric data over a reasonably flat, well-calibrated area were not available at the time of the analysis for this paper, but such a data set has recently been acquired and is currently in the early processing phase, and will be reported in future publications. The analysis below proceeds under the assumption that because the {$HHHH/VVVV$} data were taken at the same time of year over the same site, they result from similar terrain characteristics as the interferometric data taken 1 year later. Implicit also is the assumption that instrumental calibration of the {$HHHH/VVVV$} data is accurate at the 1% level or better for the two acquisition epochs. If these assumptions are in error, they will probably contribute to errors in the parameters estimated with interferometry and polarimetry.

Figure 7 shows an interferometric cross-correlation amplitude map of the part of the BOREAS Southern Study Area used in the data demonstration of parameter estimation. The correlation amplitudes range from about 0.8 to 1.0 for the 5-m TOPSAR (ping-pong) baseline, and the stands of Table 4 are numbered. The approximate coordinates of the center of the image are $-104.7°$ longitude and $53.9°$ latitude. Each stand is 100–200 m on a side, with field-measured stand heights and vegetation types as indicated in Table 5 (Saskatchewan Environment and Resource Management, report, available at http://www.eosdis.ornl.gov/, 1998). In Figure 7 the darker areas (smaller amplitudes) result from taller vegetation. Although thermal noise effects have been removed from Figure 7, the range effects in A_r have not been removed, and there is some trend toward lower correlation amplitudes at smaller incidence angles (left-hand side of the figure).

Parameters will be estimated in two modes of

analysis: (1) from the interferometric data alone and then (2) from the combined interferometric + {$HHHH/VVVV$}-ratio data set. Other polarimetric quantities will not be introduced because from Table 2, their inclusion in the analysis introduces the need to estimate more parameters which have to do with single-scatterer characteristics and not vertical vegetation structure. For the direct-ground mechanism the parameter estimates (indicated by circumflexes below) in the first mode, from the 2.5- and 5-m interferometric-baseline data alone, can be represented by (see equation (24))

$$
\begin{pmatrix} \hat{h}_v \\ \hat{z}_0 \\ \hat{\sigma}_x \\ \hat{\Delta}_{\hat{V}}^D \end{pmatrix} = \mathbf{M}_I^{-1} \begin{pmatrix} \text{2.5-m correlation amplitude} \\ \text{2.5-m correlation phase} \\ \text{5-m correlation amplitude} \\ \text{5-m correlation phase} \end{pmatrix} \equiv \mathbf{M}_I^{-1}(O_I),
$$

(30)

where $\mathbf{M}_I^{-1}$ is an operator which transforms a set of two-baseline interferometric data into the parameter estimates on the left side of (30), using $\mathbf{M}_I$ as in (24). In (30) the observation vector (O_I) is defined by (30). If the {$HHHH/VVVV$} ratio is included in the parameter estimation, at a different incidence angle θ_p, and slightly rough-surface scattering is assumed, the parameter vector becomes (from the definition of $\Delta_{\hat{V}}^D$ following (24) and (25))

$$
\begin{pmatrix} h_v \\ z_0 \\ \sigma_x \\ \Delta_{\hat{V}}^D(\theta_0) \\ \Delta_{\hat{V}}^D(\theta_p) \\ \Delta_{\hat{H}}^D(\theta_p) \end{pmatrix} \equiv \begin{pmatrix} h_v \\ z_0 \\ \sigma_x \\ \Psi \cos^4 \theta_0 \langle \alpha_{\hat{V},\hat{V}}^2(\varepsilon_r) \rangle \\ \Psi \cos^4 \theta_p \langle \alpha_{\hat{V},\hat{V}}^2(\varepsilon_r) \rangle \\ \Psi \cos^4 \theta_p \langle \alpha_{\hat{H},\hat{H}}^2(\varepsilon_r) \rangle \end{pmatrix},
$$

(31)

where the interferometry is done at incidence angle θ_0 and the parameter $\Psi \equiv k_0^4 W_P(-2k_0 \sin \theta_0, 0)/\rho_0 \langle |\hat{V} \cdot \mathbf{F}_b \cdot \hat{V}|^2 \rangle = k_0^4 W_P(-2k_0 \sin \theta_0, 0)/\rho_0 \langle |\hat{H} \cdot \mathbf{F}_b \cdot \hat{H}|^2 \rangle$ is assumed to be independent of incidence angle. That is, the roughness power spectrum is not assumed to change much when evaluated at the two incidence angles. This assumption, along with that of the slightly rough surface, is necessary to reduce the six-element parameter set in (31) to the following five-element set (there are only five observations): (1) h_v, (2) z_0, (3) σ_x, (4) Ψ, and (5) ε_r. The parameter estimation scenario becomes
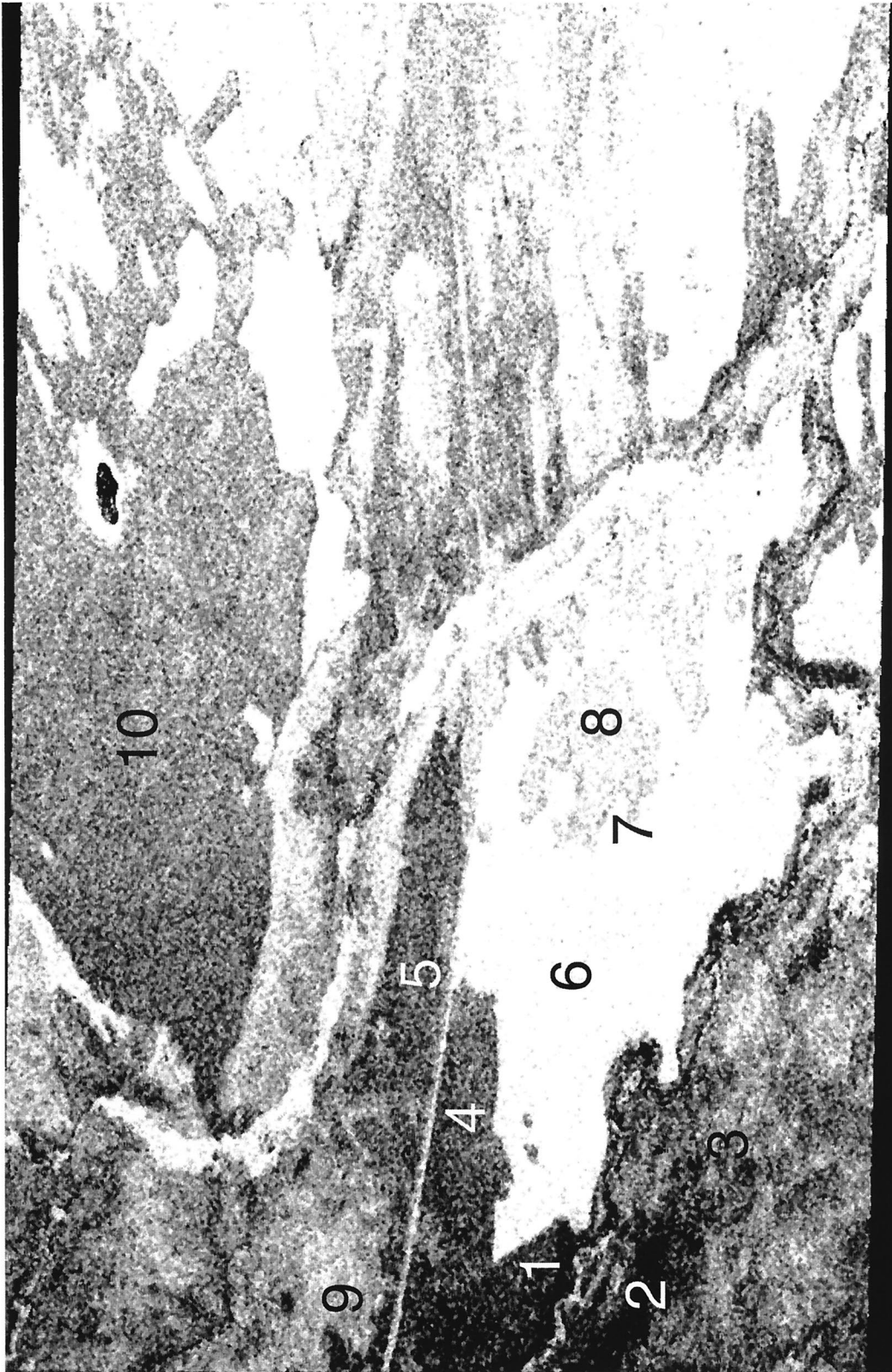
Figure 7. The correlation amplitude image for the part of the Boreal Ecosystem–Atmosphere Study (BOREAS) Southern Study Area used in the data demonstration. The numbers indicate the locations of stands, 100–200 m on a side, used in the analysis. Black in the figure corresponds to amplitudes of 0.78, and white corresponds to 1.0.

Table 5. Vegetation Height, Underlying Topography, and Ground-to-Volume Power Ratio Estimated From the BOREAS Data in Table 4

Stand	Vegetation Type	Field-Measured Tree Height, m	Tree Height Estimate, m	Topography Estimate, m	Ground/Volume Estimate
1	jack pine/spruce	19.0	16.5 (1.4)	5.6 (1.0)	0.24 (0.17)
2	aspen	20.0	22.3 (1.0)	9.0 (1.0)	0.20 (0.08)
3	spruce fir/broad leaf	16.7	13.5 (1.3)	9.6 (1.7)	0.18 (0.18)
4	jack pine	15.0	14.9 (0.2)	−1.3 (0.4)	0.25 (0.05)
5	jack pine	15.0	17.2 (5.7)	−9.0 (6.0)	0.13 (0.08)
6	clear cut	0.0	0.00 (0.4)	0.0 (0.3)	0.01 (0.14)
7	clear cut/jack pine	2.6	0.0 (1.3)	0.4 (1.0)	0.13 (>1.0)
8	jack pine/black spruce	7.3	6.9 (2.7)	−0.3 (3.0)	0.06 (0.08)
9	treed muskeg	0.0	5.6 (0.5)	−11.1 (0.4)	0.08 (0.07)
10	jack pine	15.0	25.4 (7.3)	−3.4 (7.2)	0.02 (0.03)

Standard deviations of parameter estimates are shown in parentheses, and field-measured vegetation heights and vegetation types are also shown.

$$\begin{pmatrix} \hat{h}_v \\ \hat{z}_0 \\ \hat{\sigma}_x \\ \hat{\Psi} \\ \hat{\varepsilon}_r \end{pmatrix} = \mathbf{M}_{I+P}^{-1} \begin{pmatrix} \text{2.5-m correlation amplitude} \\ \text{2.5-m correlation phase} \\ \text{5-m correlation amplitude} \\ \text{5-m correlation phase} \\ \{HHHH/VVVV\} \end{pmatrix}$$

$$\equiv \mathbf{M}_{I+P}^{-1}(O_{I+P}), \tag{32}$$

where $\mathbf{M}_{I+P}^{-1}$ is an operator which transforms a set of two-baseline interferometric data plus the zero-baseline polarimetric $\{HHHH/VVVV\}$ ratio into the parameter estimates on the left side of (32), based on (24) and (25). Since the ground dielectric constant is complex, there are actually six parameters on the left side of (32), but the imaginary part of ε_r is assumed to be $0.15 \times \text{Re}(\varepsilon_r)$, typical of soil [*Moghaddam and Saatchi*, 1995]. The last parameter ε_r effectively becomes just one parameter. It was found that estimates of other parameters were very insensitive to the assumed ratio of the real to imaginary parts of ε_r.

In either estimation scenario, (30) or (32), $\mathbf{M}_I^{-1}$ or $\mathbf{M}_{I+P}^{-1}$ are nonlinear least squares operators which, by searching parameter space as indicated in Figure 1, find the parameter estimates $\hat{h}_v$, $\hat{z}_0$, $\hat{\sigma}_x$, $\hat{\Psi}$, and $\hat{\varepsilon}_r$ which minimize (for example, for equation (32))

$$\left[(O_{I+P}) - \mathbf{M}_{I+P} \begin{pmatrix} \hat{h}_v \\ \hat{z}_0 \\ \hat{\sigma}_x \\ \hat{\Psi} \\ \hat{\varepsilon}_r \end{pmatrix} \right]^T \mathbf{C}^{-1} \left[(O_{I+P}) - \mathbf{M}_{I+P} \begin{pmatrix} \hat{h}_v \\ \hat{z}_0 \\ \hat{\sigma}_x \\ \hat{\Psi} \\ \hat{\varepsilon}_r \end{pmatrix} \right], \tag{33}$$

where $\mathbf{C}$ is the covariance matrix of the measurements in O_{I+P}. The covariance matrix is assumed to have the squares of the observation measurement errors

on the diagonals and zero everywhere else (observation errors are assumed uncorrelated). The observation errors used in (33), which are shown in parentheses in Table 4, were empirically determined by dividing each stand into sections, and they were also calculated based on the standard deviation of the mean of the distributions of each observation type within each stand. Both methods of calculating entries for $\mathbf{C}$ usually yielded about the same observation error, and in the cases where they differed, the larger value was used.

Table 5 shows the parameter estimates and standard deviations for the vegetation height, the underlying topography, and the ratio of ground to volume power, which is a function of the estimated parameters (see equations (29), (31), and (32)). This ratio is shown instead of extinction coefficient estimates, which ranged between 0.0 and 0.4 dB/m, because it seemed to be better determined and could be compared with values in the literature. Table 5 parameter estimates and standard deviations are for the interferometry + polarimetry scenario of (32). The standard deviations in Table 5 in parentheses are determined by adding Monte Carlo, Gaussian distributions of observation errors to (O_{I+P}), based on the square roots of the diagonal elements of $\mathbf{C}$. The parameter standard deviations in Table 5 result from (32) and (33) and are the error bars in the figures described below. It should be noted that in nonlinear estimation, the process of adding even symmetric noise to observations results in asymmetric distributions of parameters about the optimal values in Table 5. The asymmetric nature of the error bars is not shown in the figures which follow, because for all but the
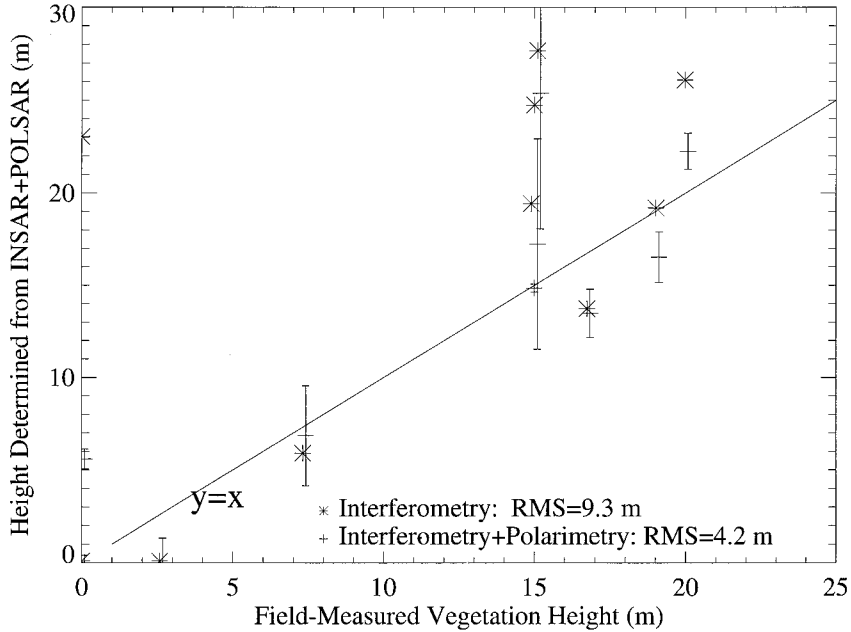
Figure 8. Vegetation height estimated from the BOREAS "interferometry" (INSAR) (asterisks) and INSAR + {$HHHH/VVVV$} ratio (plus signs) data, as a function of field-measured vegetation height.

smallest parameter values, the parameter distributions are fairly (to within about 20% of the error bar) symmetric about the estimate, and the asymmetry adds a layer of complication unnecessary for the interpretation of the results. The asymmetry, however, should be especially kept in mind for the small-value parameter estimate entries in Table 5, for which the standard deviation is larger than the value itself, for example, for tree height. The parameter distribution arising from adding observation error to the actual observations never produces a negative height, because the optimal estimate is not at the center of the parameter distribution.

Figure 8 shows the estimate of vegetation height $\hat{h}_v$ versus field-measured vegetation height for the 10 stands considered. The asterisks correspond to the interferometry-only parameter estimation scenario (30), and the plus signs correspond to the interferometry + polarimetry estimation scenario (32). The single data point which seemed to come from specular scattering ({$HHHH/VVVV$} > 1) was analyzed with specular estimation scenarios, analogous to (30) and (32). The rms scatter about the field-measured values, indicated by the line $y = x$, for interferometry alone is 9.3 m and for interferometry + polarimetry is 4.2 m. The field-measured values were binned in 5-m

bins, suggesting that the actual scatter of the parameter estimates could be as low as 3.2 m. Although not shown, if the ground contribution were not included, almost all estimates of h_v increase, as expected from Figure 6a. The rms scatter for the randomly oriented volume alone becomes very large, ~20 m, owing largely to the gross overestimation of h_v for two of the data points.

In Figure 8 the parameter estimation of h_v is improved by adding the polarimetry to the multibaseline interferometry. The reduced χ^2 about the $y = x$ line in Figure 8 is 13, suggesting that the actual scatter is about 4 times that expected from modeled parameter errors. The possibilities for accounting for this excess error fall into two general categories: The first is model deficiencies (in $\mathbf{M}_{I+P}$ based on (24) and (25)), such as oriented volume effects which would alter the {$HHHH/VVVV$} ratio (see Figure 6b), the assumed equivalence of the surface roughness power spectrum for the interferometry and polarimetry incidence angles (i.e., $W_P(-2k_0 \sin \theta_0, 0) = W_P(-2k_0 \sin \theta_p, 0)$), unmodeled temporal changes in terrain between the interferometric and polarimetric data acquisitions, and unmodeled multilayer vertical structure. The second general category of unmodeled error is systematic, instrumental error in the
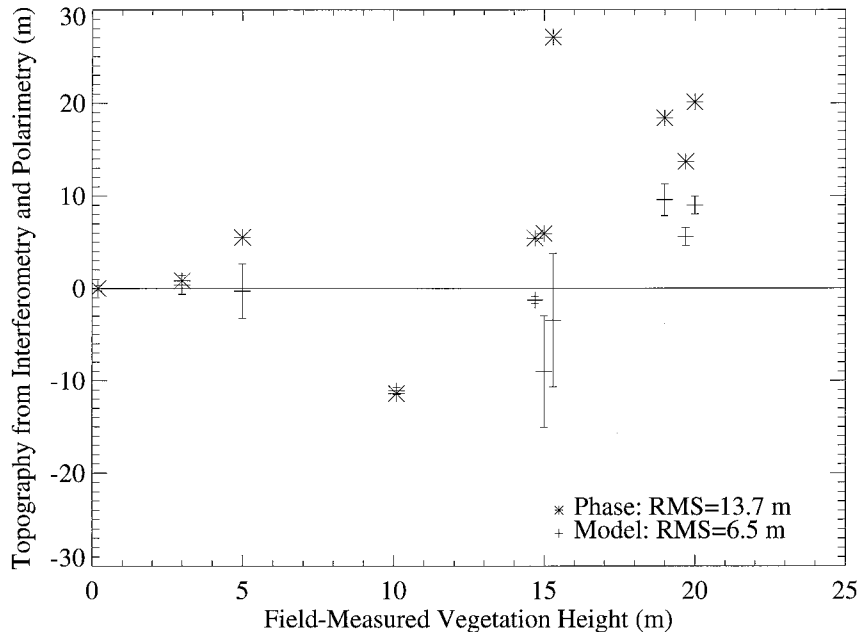
Figure 9.   Underlying topography estimated from the BOREAS data, as a function of field-measured vegetation height. Average topography is zero, indicated by the horizontal line.

data not reflected in the scatters used to arrive at error estimates, such as phase offset and ramp errors, cross-correlation amplitude miscalibration, and imperfect removal of the noise or range (A_r) decorrelation effects.

Figure 9 shows the underlying topography as a function of the field-measured vegetation height. This region is flat to within ± 5 m, and the horizontal line at zero shows the approximate correct topography. The asterisks show the topography inferred from the long-baseline phase alone, by dividing by α_z. This is the standard method for arriving at the bare-surface topography, but it will produce errors of the order of the vegetation height for vegetated land surfaces. The asterisks indeed show departures from the zero line of the order of the vegetation height, and the rms error about zero is 13.7 m. The plus signs show the underlying topography estimated as the $\hat{z}_0$ parameter in (32), with interferometry and polarimetry. The rms scatter about zero is reduced by a factor of 2, to 6.5 m. The reduced χ^2 about the zero line is very poor, about 120, indicating either that unmodeled errors strongly affect the z_0 parameter or there is some actual topography in the scene at the 7-m level.

Figure 10 shows another example of a parameter estimable from a combined interferometric and pola-

rimetric data set. It is the ratio of received ground-to-volume power for the interferometric incidence angle, determined from the parameters in the combined interferometric and polarimetric estimation scenario represented by (32). This quantity, R_{g-v}, is a structure parameter in that it gives the ratio of received powers from two spatially distinct components of the vegetated land surface. The ratio is calculated from the parameters in (32) by inserting them into (29). The ratio is plotted versus the radar-estimated vegetation height. The horizontal line is the weighted average value of the ratio, which was 0.124. Field measurements of the ratio of ground to volume power were not available for the stands reported here. On the basis of field measurements at the site, forward modeling, and polarimetric observations [*Moghaddam and Saatchi*, 1995; *Freeman and Durden*, 1998], ratios of ground to volume power of the order of 10% are expected, and the ratios shown in Figure 10 are thus plausible. The number of ratios significantly different from zero in Figure 10 again suggests that ground contributions are detectable at C band. The reduced χ^2 of the parameters about the average value was smaller than that about a linear fit. Although there is the suggestion of a trend toward higher ratios at higher tree heights, which could be
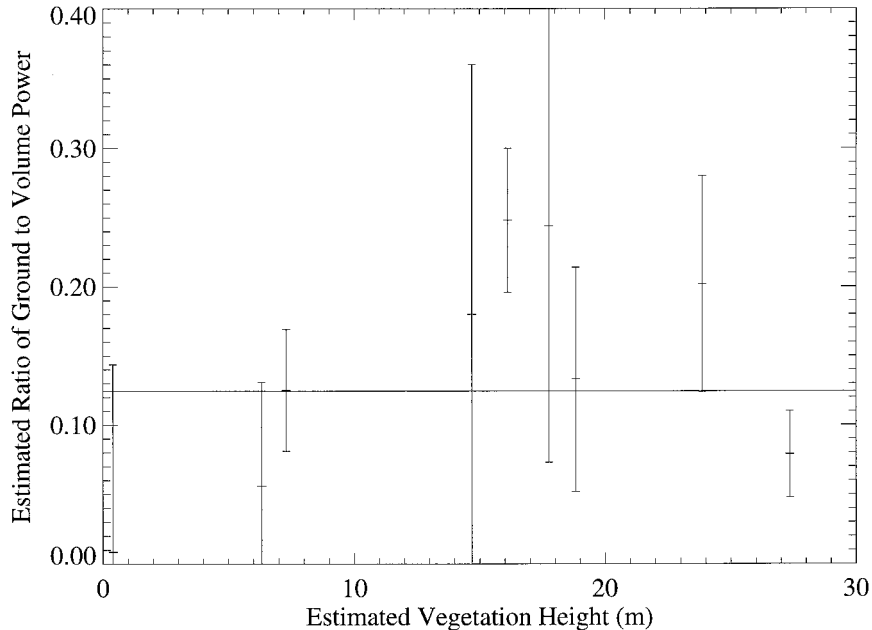
Figure 10. Ratio of ground to volume power estimated from the BOREAS data as a function of estimated vegetation height.

explained, for example, by a concurrent reduction in tree surface density (so the ground would be more accessible to the incident radiation), this trend is not statistically significant. Although not shown, ground-to-volume power ratios obtained from interferometry were, for some data points, a factor of 10 less accurate, which was reflected in ratios of the order of 2.0 and correspondingly large error bars. The {*HHHH/VVVV*} ratio was very important for constraining this parameter to the reasonable range in Figure 10.

In addition to the levels of agreement with expectation from field measurements, an indication of the accuracy of the models used in the parameter estimation results from comparing the model data to the actual data. The "model data" are those which result when the optimal parameter estimates, including those in Table 5, are used in the model to generate observations. The resulting model interferometric correlation amplitudes are typically within 0.5% of those in the data, which is also of the order of the correlation-amplitude observation error (see Table 4). The amplitudes are therefore fit well by the model M_{I+P}. The discrepancy between model phase and data phase is of the order of 1°–4°, which is frequently considerably larger than the phase observation errors

given in Table 4. This indicates that the procedure described above may underestimate phase errors in the data. Calibration approaches in multialtitude data sets are being pursued to find and correct systematic phase and amplitude errors in future data sets.

4. Summary and Future Acquisition and Estimation Scenarios

This paper casts the combining of interferometric and polarimetric radar as the measurement of a general polarimetric interferometric cross correlation (equation (1)), from which parameters pertaining to vegetation vertical structure can be estimated. In order to construct physical models of the cross correlation which depend on a small number of vegetation and surface parameters, three simple physical mechanisms were considered: (1) the randomly oriented volume, (2) the randomly oriented volume with a ground return, both specular and direct, and (3) the oriented volume. The ground surfaces were always taken to be horizontal. For each mechanism, up to five parameters were identified on which the interferometric (all polarizations the same) and polarimetric (zero-baseline) cross correlations depend. The {*HHHH/VVVV*} ratio was the only polarimetric

quantity used in parameter estimation, because it was shown that adding other polarimetric cross correlations without the analogous fully polarimetric interferometric cross-correlation observations introduced parameters which pertained to single-scatterer characteristics and did not enhance the accuracy of vertical-structure parameters. For the randomly oriented volume + direct-ground return, the dependence of the interferometric cross-correlation amplitude and $\{HHHH/VVVV\}$ ratio on vegetation height was shown as an example of observation sensitivity to structure parameters. The sensitivity analysis suggested that few-meter vegetation height accuracy would be possible if the model accurately described the terrain. The sensitivity of the $\{HHHH/VVVV\}$ ratio to height implied that the addition of this ratio to the interferometric data should improve vegetation parameter estimation, if the slightly rough, direct-ground mechanism was assumed (so that the polarimetric response can be characterized). Vegetation heights, underlying topography, and the ratio of ground to volume power were estimated from two-baseline TOPSAR interferometric data plus $\{HHHH/VVVV\}$ ratios taken over the BOREAS Southern Study Area. The accuracy of vegetation heights estimated from two-baseline interferometry alone, with a four-parameter fit, was about 9.3 m, as determined by comparison with field measurements. When the $\{HHHH/VVVV\}$ ratio was included in the analysis with the above assumption, the estimation accuracy improved to 4.2 m with a five-parameter fit. The underlying topography of the part of the BOREAS Southern Study Area used is flat to within ± 5 m, and using the parameter estimation approach reduced the rms scatter of the estimated topography inferred from topographic phase alone from 13.7 to 6.5 m. Although no field measurements were available for the ratio of ground to volume power, which is a function of estimated parameters, it was estimated from interferometry and polarimetry to have an average value of 12%, which is reasonable given expectations from measurements at the site. Without the $\{HHHH/VVVV\}$, i.e., with interferometry alone, the accuracy and value of this parameter were as high as 2.0 for some stands, suggesting that the $\{HHHH/VVVV\}$ ratio seems to play a crucial role in the estimation of this parameter. The data demonstrations in this paper show the feasibility of combining interferometry and polarimetry, but many simplifying assumptions were made in modeling the data, many

of which would not be necessary with more complete data sets, including polarimetric interferometry.

A central conclusion of this paper is that fully polarimetric interferometry will enable parameter estimation with more realistic and less constrained models. Vertical-structure parameters estimated from polarimetric interferometry will therefore potentially be more accurate than those estimated from the combination of interferometry and zero-baseline polarimetry. If ground slopes and vertical profiles of vegetation density or extinction are added to the parameter list, multibaseline polarimetric interferometry will probably be required for their estimation. A multialtitude interferometric + zero-baseline polarimetric data set has been collected over central Oregon to evaluate the additional parameter estimation accuracy achieved. Because α_z, which determines the interferometric sensitivity, is proportional to the baseline length divided by the altitude, multialtitude data are equivalent to multibaseline data. Coupled with the ping-pong capability, this data set should provide four unique baselines ranging from 2.5 to 20 m. Data analysis will begin on that experiment soon. Data were also acquired in a second multialtitude experiment with fully polarimetric TOPSAR in June 1999, in order to further test the hypothesis that vertical-structure parameter estimation will improve with these new data types. It was mentioned that the analysis of oriented volumes may be tremendously simplified with polarimetric interferometry. The analysis of more complete data sets may also enable accounting for more realistic features of vegetated land surfaces than presented in the three models in this paper. For example, terrain slopes affect interferometric correlation amplitudes and phases by changing the distribution of vegetation and polarimetric quantities by changing the Fresnel and direct-surface reflection scattering mechanisms [*Schuler et al.*, 1998]. The estimation of terrain slopes as parameters will be attempted with fully polarimetric multibaseline interferometry. Vegetation vertical-structure parameters in addition to height, for example, height-to-base-of-live-crown [*Treuhaft et al.*, 1997], may be estimable from the more complete data sets. One modeling approach could, for example, accommodate different estimable polarimetric attributes at each of several layers in the vegetation.

In addition to fully polarimetric, multibaseline radar interferometry, future observation vectors from which vegetation structure parameters may be estimated (as in equations (30) and (32)) include other

remote sensing data types. Multifrequency radar interferometry, available, for example, from TOPSAR and GeoSAR [*Thompson et al.*, 1999], will augment the observation vector. Like the addition of polarization information, the addition of different frequencies adds diverse sensitivities to the vertical components of the scattering scene. Optical remote sensing data may also be added to the observation vector. For example, lidar profiling techniques [*Means et al.*, 1999] can potentially supply accurate vertical structure information over limited spatial domains and may be useful in constraining parameters estimated from radar over much broader regions, thereby improving parameter accuracy. Including lidar and microwave observations in a generalized observation vector may help to minimize errors inherent in each technique. Hyperspectral data and radiative transfer inversion techniques may also be used to estimate leaf area and the horizontal cover fraction of live vegetation [*Asner et al.*, 1998]. These parameters derived from hyperspectral optical data may be combined with the profiling potential of radar [*Treuhaft et al.*, 1997] to determine, for example, vertical profiles of leaf area and leaf area density. The augmentation of the observation vector with data types sensitive to vertical structure, with the associated development of the required simple (easily parameterized) model scenarios, will improve vertical-structure parameter accuracies beyond those reported in the preliminary demonstrations in this paper.

Appendix A: Ground-Volume and Volume-Ground Contributions to the Received Field

In order to calculate the cross correlation (4) for the specular ground-volume and volume-ground mechanism in the presence of a randomly oriented volume, here we calculate the specular contribution to the field $\vec{E}_{\hat{t}_1}(\vec{R}_1, \omega_0; \vec{R})$ from a volume scatterer at $\vec{R}$, expressed in (10). This field will then be inserted into (4) to arrive at the cross correlation, as shown in Appendix B. The field $\vec{E}_{\hat{t}_1}(\vec{R}_1, \omega_0; \vec{R})$ is that received at $\vec{R}_1$ due to a volume scattering element at $\vec{R}$. The direct backscattered volume contribution, without the ground mechanism, is as in (5) or $\vec{E}_v$ in (10).

Deriving the specular ground contribution entails first considering the average field incident on the scatterer at $\vec{R}$ when the specular ground reflection is

significant. With a specular contribution from the ground this incident field will have two contributions:

$$\langle \vec{E}_{\hat{t}_1}(\vec{R}, \omega_0) \rangle = \langle \vec{E}_{\hat{t}_1}(\vec{R}, \omega_0; \vec{R}_1) \rangle + \langle \vec{E}_{\hat{t}_1}(\vec{R}, \omega_0; \vec{R}_{sp1,\vec{R}}) \rangle,$$

(A1)

where the first term is the average wave propagating directly from the transmitter to $\vec{R}$ and the second term is the ground-reflected contribution, and $\vec{R}_{sp1,\vec{R}}$ is the specular reflection point for vegetation at $\vec{R}$, as shown in Figure 5b. Using the Kirchhoff approximation for a rough surface with zero average slope, the second term can be expressed as an integral over the surface [*Beckmann and Spizzichino*, 1963], with an additional integration over the vertical direction to describe the stochastic surface roughness. Assuming that $\hat{t}_1$ is either $\hat{H}$ or $\hat{V}$ simplifies the specular incident field, and, in any case, $\hat{t}_1$ can be expressed in these eigenpolarizations of the ground-reflection matrix (11). Accounting for the volume propagation effects (see equation (5)) from the transmitter to the specular point, and from the specular point to the volume element at $\vec{R}$, the average field incident on $\vec{R}$ from the specular reflection point is

$$\langle \vec{E}_{\hat{t}_1}(\vec{R}, \omega_0; \vec{R}_{sp1,\vec{R}}) \rangle$$

$$= \frac{ik_0 \hat{t}_1 e^{ik_0|\vec{R} - \vec{R}_{sp1,\vec{R}}|}}{4\pi|\vec{R} - \vec{R}_{sp1,\vec{R}}|} \exp\left[\frac{2\pi i\rho_0 \langle \hat{t}_1 \cdot \mathbf{F}_f \cdot \hat{t}_1 \rangle (h_v + z)}{k_0 \cos\theta_{sp1,\vec{R}}}\right]$$

$$\times \int P(z', z_0)\, dz' \int dx'\, dy'\, [\langle R_{\hat{t}_1}(\theta_{sp1,\vec{R}}) \rangle)(\hat{k}_{\text{inc}}$$

$$- \hat{k}_{\text{ref}}) \cdot \hat{n} - (\hat{k}_{\text{inc}} + \hat{k}_{\text{ref}}) \cdot \hat{n}] e^{i(\vec{k}_{\text{inc}} - \vec{k}_{\text{ref}}) \cdot \vec{R}'}, \quad (A2)$$

where $\langle R_{\hat{t}_1}(\theta_{sp1,\vec{R}}) \rangle$ is the average specular reflection coefficient for polarization $\hat{t}_1$; $\vec{R}'(x', y', z'(x', y'))$ is the surface integration variable; $\vec{k}_{\text{inc}} \equiv \vec{R}_{sp1,\vec{R}} - \vec{R}_1$; $\vec{k}_{\text{ref}} \equiv \vec{R} - \vec{R}_{sp1,\vec{R}}$; $\hat{n}$ is a surface unit normal vector; and $P(z', z_0)$ is the probability density of the surface having a fluctuation of the z coordinate of $z' - z_0$ about a reference altitude z_0. In (A2), z is the vertical coordinate of the volume element at $\vec{R}$. If, as given by *Beckmann and Spizzichino* [1963], $P(z', z_0)$ is taken to be of the Gaussian form $\exp[-(z' - z_0)^2/2\sigma_z^2]/\sqrt{2\pi}\,\sigma_z$, with σ_z being the standard deviation of surface vertical fluctuations, the method of stationary phase [e.g., *Ishimaru*, 1978] applied to (A2) yields

$\langle \vec{E}_{\hat{t}_1}(\vec{R}, \omega_0; \vec{R}_{sp1,\vec{R}}) \rangle$

$$= \frac{\langle \mathbf{R}(\theta_{sp1,\vec{R}}) \rangle \hat{t}_1}{|\vec{R}_1 - \vec{R}_{sp1,\vec{R}}| + |\vec{R} - \vec{R}_{sp1,\vec{R}}|} e^{ik_0[|\vec{R}_1 - \vec{R}_{sp1,\vec{R}}| + |\vec{R} - \vec{R}_{sp1,\vec{R}}|]}$$

$$\times \exp\left[\frac{2\pi i \rho_0 \langle \hat{t}_1 \cdot \mathbf{F}_f \cdot \hat{t}_1 \rangle (h_v + z)}{k_0 \cos \theta_{sp1,\vec{R}}}\right] \frac{1}{\sqrt{2\pi} \, \sigma_z}$$

$$\cdot \int_{-\infty}^{\infty} \exp\left[-\frac{(z' - z_0)^2}{2\sigma_z^2} - 2ik_0 \cos \theta_0 (z' - z_0)\right] dz'$$

$$\approx A \langle \mathbf{R}(\theta_{sp1,\vec{R}}) \rangle \cdot \hat{t}_1 \Gamma_{\text{rough}} e^{ik_0[|\vec{R}_1 - \vec{R}_{sp1,\vec{R}}| + |\vec{R} - \vec{R}_{sp1,\vec{R}}|]}$$

$$\cdot \exp\left[\frac{2\pi i \rho_0 \langle \hat{t}_1 \cdot \mathbf{F}_f \cdot \hat{t}_1 \rangle (h_v + z)}{k_0 \cos \theta_{sp1,\vec{R}}}\right], \tag{A3}$$

with Γ_{rough} as in (12), and the distance from the transmitter to the surface plus the distance from the surface to $\vec{R}$ has been approximated by A. In (A3) the result has been generalized for arbitrary $\hat{t}_1$ by including the average ground-reflection matrix $\langle \mathbf{R}(\theta_{sp1,\vec{R}}) \rangle$.

The field incident at the volume scatterer at $\vec{R}$ must now be multiplied by the specular scattering matrix $\mathbf{F}_{\vec{R}_{sp1,\vec{R}} \rightarrow \vec{R}_1}$, a spherical-wave propagation term, and terms accounting for propagation from $\vec{R}$ directly back to the receiver at $\vec{R}_1$ (no further ground interaction), yielding for the ground-volume contribution to (10):

$$\vec{E}_{\hat{t}_1}(\vec{R}_1, \omega_0; \vec{R})(\text{G} - \text{V})$$

$$= A^2 \mathbf{F}_{\vec{R}_{sp1,\vec{R}} \rightarrow \vec{R}_1} \langle \mathbf{R}(\theta_{sp1,\vec{R}}) \rangle \cdot \hat{t}_1 \Gamma_{\text{rough}}$$

$$\cdot \exp\ [ik_0[|\vec{R}_1 - \vec{R}_{sp1,\vec{R}}| + |\vec{R} - \vec{R}_{sp1,\vec{R}}| + |\vec{R}_1 - \vec{R}|]]$$

$$\cdot \exp\left[\frac{4\pi i \rho_0 \langle \hat{t}_1 \cdot \mathbf{F}_f \cdot \hat{t}_1 \rangle h_v}{k_0 \cos \theta_{sp1,\vec{R}}}\right]. \tag{A4}$$

The volume-ground term in (10) results from using the first term in (A1) as the incident field on $\vec{R}$, multiplying by the volume specular scattering matrix $\mathbf{F}_{\vec{R} \rightarrow \vec{R}_{sp1,\vec{R}}}$, and then allowing the wave to interact with the volume and the ground on the way back to $\vec{R}_1$.

Appendix B: Cross Correlation for the Randomly Oriented Volume and Specular Ground Return

Here we derive (13) in detail. The two fields which must be introduced into (4), with volume contributions (5), and ground-volume and volume-ground

contributions (10) are for transmission at polarization $\hat{t}_1$ from $\vec{R}_1$ and reception at end 1 of the baseline

$$\vec{E}_{\hat{t}_1}(\vec{R}_1, \omega_0; \vec{R}) = A^2 \mathbf{F}_{b,\vec{R}} \cdot \hat{t}_1$$

$$\cdot \exp\left[2ik_0|\vec{R}_1 - \vec{R}| + \frac{4\pi i \rho_0 \langle \hat{t}_1 \cdot \mathbf{F}_f \cdot \hat{t}_1 \rangle (h_v - z)}{k_0 \cos \theta_{sp1,\vec{R}}}\right] (\text{V})$$

$$+ A^2 \exp\left[ik_0\{P_1(\vec{R})\} + \frac{4\pi i \rho_0 \langle \hat{t}_1 \cdot \mathbf{F}_f \cdot \hat{t}_1 \rangle h_v}{k_0 \cos \theta_{sp1,\vec{R}}}\right] \Gamma_{\text{rough}}$$

$$\times \mathbf{F}_{\vec{R}_{sp,\vec{R}} \rightarrow \vec{R}_1} \langle \mathbf{R}(\theta_{sp1,\vec{R}}) \rangle \cdot \hat{t}_1 \ (\text{G} - \text{V})$$

$$+ A^2 \exp\left[ik_0\{P_1(\vec{R})\} + \frac{4\pi i \rho_0 \langle \hat{t}_1 \cdot \mathbf{F}_f \cdot \hat{t}_1 \rangle h_v}{k_0 \cos \theta_{sp1,\vec{R}}}\right] \Gamma_{\text{rough}}$$

$$\times \langle \mathbf{R}(\theta_{sp1,\vec{R}}) \rangle \cdot \mathbf{F}_{\vec{R}_1 \rightarrow \vec{R}_{sp1,\vec{R}}} \hat{t}_1 \ (\text{V} - \text{G}). \tag{B1}$$

For transmission at polarization $\hat{t}_2$ at end 1 of the baseline (assume that there is a transmitter only at end 1) and reception at end 2 of the baseline, with $\vec{R}_{spi,\vec{R}}$ the specular point between $\vec{R}_i$ and $\vec{R}$ (see Figure B1),

$$\vec{E}_{\hat{t}_2}(\vec{R}_2, \omega_0; \vec{R}) = A^2 \mathbf{F}_{B,\vec{R}} \cdot \hat{t}_2 \exp\left[ik_0\{|\vec{R}_1 - \vec{R}|\right.$$

$$\left. + |\vec{R} - \vec{R}_2|\} + \frac{4\pi i \rho_0 \langle \hat{t}_1 \cdot \mathbf{F}_f \cdot \hat{t}_1 \rangle (h_v - z)}{k_0 \cos \theta_{\vec{R}}}\right] (\text{V})$$

$$+ A^2 \exp\left[ik_0\{P_1(\vec{R}) + |\vec{R}_2 - \vec{R}| - |\vec{R}_1 - \vec{R}|\}\right.$$

$$\left. + \frac{4\pi i \rho_0 \langle \hat{t}_1 \cdot \mathbf{F}_f \cdot \hat{t}_1 \rangle h_v}{k_0 \cos \theta_{sp1,\vec{R}}}\right] \Gamma_{\text{rough}}$$

$$\times \mathbf{F}_{\vec{R}_{sp1,\vec{R}} \rightarrow \vec{R}_1} \langle \mathbf{R}(\theta_{sp1,\vec{R}}) \rangle_{medg} \cdot \hat{t}_2 \ (\text{G} - \text{V})$$

$$+ A^2 \exp\left[ik_0\{P_2(\vec{R}) + |\vec{R}_1 - \vec{R}| - |\vec{R}_2 - \vec{R}|\}\right.$$

$$\left. + \frac{4\pi i \rho_0 \langle \hat{t}_1 \cdot \mathbf{F}_f \cdot \hat{t}_1 \rangle h_v}{k_0 \cos \theta_{sp1,\vec{R}}}\right] \Gamma_{\text{rough}}$$

$$\times \langle \mathbf{R}(\theta_{sp1,\vec{R}}) \rangle \cdot \mathbf{F}_{\vec{R}_1 \rightarrow \vec{R}_{sp1,\vec{R}}} \hat{t}_2 \ (\text{V} - \text{G}), \tag{B2}$$

where the following definitions of round-trip range and interferometric phase were used in (B1) and (B2):

$$P_1(\vec{R}) \equiv |\vec{R}_{sp1,\vec{R}} - \vec{R}_1| + |\vec{R} - \vec{R}_{sp1,\vec{R}}| + |\vec{R}_1 - \vec{R}|$$

$$\approx 2|\vec{R}_2 - \vec{R}(x, y, z_0)|$$
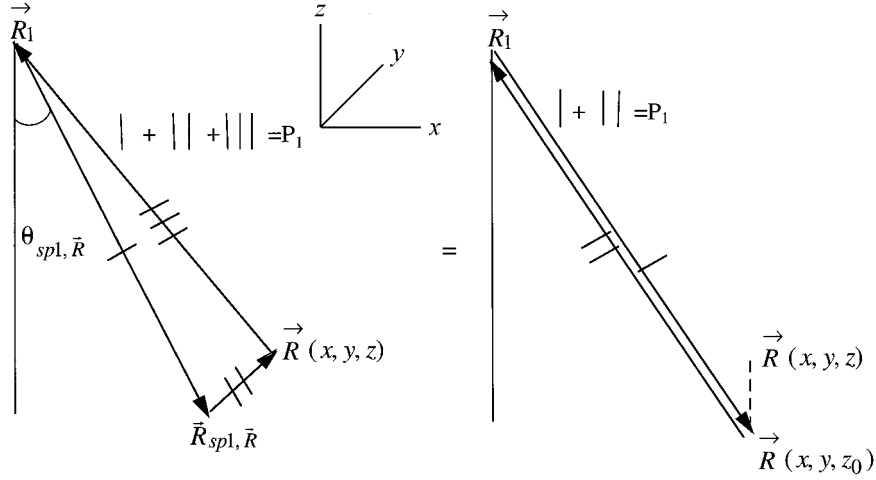
Figure B1. The specular propagation path P_1, as defined in equation (B3). On the left side, three components of the specular bounce path are shown: from the transmitter at $\vec{R}_1$ to the specular point $\vec{R}_{sp1,\vec{R}}$ (single bar), from $\vec{R}_{sp1,\vec{R}}$ to the volume element at $\vec{R}(x, y, z)$ (double bars), and from $\vec{R}(x, y, z)$ back to the receiver at $\vec{R}_1$ (triple bars). The right side shows the equivalent path from $\vec{R}_1$ to a point directly below the volume element at $\vec{R}(x, y, z_0)$ on the ground (single bar) and back from $\vec{R}(x, y, z_0)$ to $\vec{R}_1$ (double bars).

$$P_2(\vec{R}) \equiv |\vec{R}_{sp2,\vec{R}} - \vec{R}_2| + |\vec{R} - \vec{R}_{sp2,\vec{R}}| + |\vec{R}_2 - \vec{R}|$$

$$\approx 2|\vec{R}_2 - \vec{R}(x, y, z_0)|$$

$$\phi(\vec{R}) \equiv k_0|\vec{R}_1 - \vec{R}| - |\vec{R}_2 - \vec{R}| \equiv k_0(|\vec{r}_1| - |\vec{r}_2|) \qquad \text{(B3)}$$

$$\equiv k_0(r_1 - r_2).$$

Note that $\langle R(\theta_{sp1,\vec{R}}) \rangle$ and $\mathbf{F}_{R_{sp1,\vec{R}} \to R_1}$ have been assumed equal to the corresponding values for the $\vec{R}_{sp2,\vec{R}}$ specular point. In (B3) the first two equations show that the defined round-trip propagation distance is approximately equal to the round-trip propagation distance to a point on the ground (x, y, z_0) directly below the volume scatterer at $\vec{R}$ (see Figure B1). This approximation is accurate at the level of the total path length $\times (h_v/\text{radar altitude})^2$, or about 1 cm for TOPSAR. This approximation is equivalent to about a 0.2° interferometric phase error on a 5-m baseline at 8-km radar altitude at C band (TOPSAR ping-pong), which introduces few-centimeter errors in height determination and is therefore negligible; this error will be smaller still for spaceborne systems. The cross correlation of the Fourier field components needed for insertion in (4) results from taking the inner product of (B1) with the receive polarization at end 1 of the baseline $\hat{p}_1$ and cross correlating with the inner product of $\hat{p}_2$ with (B2), yielding

$$\langle \hat{p}_1 \cdot \vec{E}_{\hat{t}_1}(\vec{R}_1, \omega_0; \vec{R}) \hat{p}_2^* \cdot \vec{E}_{\hat{t}_2}^*(\vec{R}_2, \omega_0; \vec{R}) \rangle$$

$$= A^4 \exp\left[\frac{-2\sigma_x h_v}{\cos \theta_{\vec{R}}}\right]$$

$$\times \{\langle (\hat{p}_1 \cdot \mathbf{F}_{b,\vec{R}} \cdot \hat{t}_1)(\hat{p}_2^* \cdot \mathbf{F}_{B,\vec{R}}^* \cdot \hat{t}_2) \rangle \exp[i\phi(\vec{R})] \, (\text{V} * \text{V})$$

$$+ \Gamma_{\text{rough}}^2 \langle (\hat{p}_1 \cdot \mathbf{F}_{\vec{R}_{sp1,\vec{R}} \to \vec{R}_1} \langle \mathbf{R}(\theta_{sp1,\vec{R}}) \rangle \cdot \hat{t}_1)$$

$$\cdot (\hat{p}_2^* \cdot \mathbf{F}_{\vec{R}_{sp1,\vec{R}} \to \vec{R}_1}^* \langle \mathbf{R}^*(\theta_{sp1,\vec{R}}) \rangle \cdot \hat{t}_2) \rangle$$

$$\times \exp[i\phi(\vec{R})] \, (\text{G} - \text{V}) * (\text{G} - \text{V})$$

$$+ \Gamma_{\text{rough}}^2 \langle (\hat{p}_1 \cdot \mathbf{F}_{\vec{R}_{sp1,\vec{R}} \to \vec{R}_1} \langle \mathbf{R}(\theta_{sp1,\vec{R}}) \rangle \cdot \hat{t}_1)$$

$$\cdot (\hat{p}_2 \cdot \langle \mathbf{R}^*(\theta_{sp1,\vec{R}}) \rangle \cdot \mathbf{F}_{\vec{R}_1 \to \vec{R}_{sp1,\vec{R}}}^* \cdot \hat{t}_2) \rangle$$

$$\times \exp[ik_0\{P_1(\vec{R}) - P_2(\vec{R}) - i\phi(\vec{R})](\text{G} - \text{V}) * (\text{V} - \text{G})$$

$$+ \Gamma_{\text{rough}}^2 \langle (\hat{p}_1 \cdot \langle \mathbf{R}(\theta_{sp1,\vec{R}}) \rangle \cdot \mathbf{F}_{\vec{R}_1 \to \vec{R}_{sp1,\vec{R}}} \cdot \hat{t}_1)$$

$$\cdot (\hat{p}_2^* \cdot \mathbf{F}_{\vec{R}_{sp1,\vec{R}} \to \vec{R}_1}^* \langle \mathbf{R}^*(\theta_{sp1,\vec{R}}) \rangle \cdot \hat{t}_2^*) \rangle$$

$$\times \exp[i\phi(\vec{R})] \, (\text{V} - \text{G}) * (\text{G} - \text{V})$$

$$+ \Gamma_{\text{rough}}^2 \langle (\hat{p}_1 \cdot \langle \mathbf{R}(\theta_{sp1,\vec{R}}) \rangle \cdot \mathbf{F}_{\vec{R}_1 \to \vec{R}_{sp1,\vec{R}}} \cdot \hat{t}_1)$$

$\cdot (\hat{p}_2^* \cdot \langle \mathbf{R}^*(\theta_{sp1,\bar{R}}) \rangle \cdot \mathbf{F}^*_{R_1 \to \bar{R}_{sp1,\bar{R}}} \cdot \hat{t}_2^*) \rangle$

$\times \exp [ik_0\{P_1(\bar{R}) - P_2(\bar{R})\} - i\phi(\bar{R})]\}$

$\cdot (V - G) * (V - G).$ \hfill (B4)

Two types of partial derivatives of phase will occur in the simplification of (B4). They are the derivatives used by *Treuhaft et al.* [1996] using the (r_1, z, η) coordinate system and new derivatives introduced here using the (x, y, z) coordinate system necessary to treat the specular mechanism. Both sets of derivatives result from Appendix A of *Treuhaft et al.* [1996] and are shown in (B5) and (B6) below, with B being the baseline length, δ being the angle between the baseline and the horizontal, and $|_0$ indicating evaluation at the center of the range resolution cell, on the ground at $\bar{R} = \bar{R}_0$:

$$\alpha_r \equiv k_0 \left(\frac{\partial(r_1 - r_2)}{\partial r_1} \right)_{z,\eta} \Big|_0 = \frac{k_0 B \cos(\theta_0 - \delta) \cos \theta_0}{r_0 \sin \theta_0}$$

$$\alpha_z \equiv k_0 \left(\frac{\partial(r_1 - r_2)}{\partial z} \right)_{r_1,\eta} \Big|_0 = \frac{k_0 B \cos(\theta_0 - \delta)}{r_0 \sin \theta_0}$$

$$\alpha_\eta \equiv k_0 \left(\frac{\partial(r_1 - r_2)}{\partial \eta} \right)_{r_1,z} \Big|_0 = -k_0 B \sin \theta_0 \sin \eta_0 \cos \delta = 0.$$
\hfill (B5)

The derivatives in the rectangular coordinates are

$$\kappa_x \equiv k_0 \left(\frac{\partial(r_1 - r_2)}{\partial x} \right)_{y,z} \Big|_0 = \frac{k_0 B \cos \theta_0 \cos(\theta_0 - \delta)}{r_0}$$

$$\kappa_y \equiv k_0 \left(\frac{\partial(r_1 - r_2)}{\partial y} \right)_{x,z} \Big|_0$$

$$= \frac{k_0 B \sin(\delta - \theta_0) \sin \theta_0 \sin \eta_0}{r_0} = 0$$

$$\kappa_z \equiv k_0 \left(\frac{\partial(r_1 - r_2)}{\partial z} \right)_{x,y} \Big|_0 = \frac{k_0 B \sin \theta_0 \cos(\theta_0 - \delta)}{r_0},$$
\hfill (B6)

noting from (B3) that

$$k_0(P_1(\bar{R}) - P_2(\bar{R})) = 2\phi(\bar{R}(x, y, z_0))$$

$$\phi(\bar{R}) \approx \phi(\bar{R}(x, y, z_0)) + \kappa_z(z - z_0)$$

$$\Rightarrow k_0(P_1(\bar{R}) - P_2(\bar{R})) - \phi(\bar{R})$$

$$= \phi(\bar{R}(x, y, z_0)) - \kappa_z(z - z_0).$$
\hfill (B7)

The dependence on the rectangular-coordinate partial derivative results because the P_1 and P_2 path lengths depend on the rectangular x, y at $z = z_0$. Because of (B7) and because the argument of $\vec{E}\hat{\imath}_1(\bar{R}_1, \omega_0; \bar{R})$ needed for insertion in W_r in (4) depends on P_1 (and not on $\bar{R}_1 - \bar{R}$, as for the volume backscattering case), the Taylor expansion of the phase about the reference point must be done in rectangular coordinates for the specular terms. The cross correlation of the Fourier components in (B4) therefore becomes

$$\langle \hat{p}_1 \cdot \vec{E}_{\hat{\imath}_1}(\bar{R}_1, \omega_0; \bar{R}) \hat{p}_2^* \cdot \vec{E}^*_{\hat{\imath}_2}(\bar{R}_2, \omega_0; \bar{R}) \rangle = A^4 e^{i\phi_0(z_0)}$$

$$\cdot \exp \left[\frac{-2\sigma_x h_v}{\cos \theta_{\bar{R}}} \right] \times \{ \langle (\hat{p}_1 \cdot \mathbf{F}_{b,\bar{R}} \cdot \hat{t}_1)(\hat{p}_2^* \cdot \mathbf{F}^*_{b,\bar{R}} \cdot \hat{t}_2^*) \rangle$$

$$\cdot \exp [i\alpha_r(r_1 - r_0) + i\alpha_z(z - z_0)] (V * V)$$

$$+ \Gamma^2_{\text{rough}} \langle (\hat{p}_1 \cdot \mathbf{F}_{\bar{R}_{sp1,\bar{R}} \to \bar{R}_1} \langle \mathbf{R}(\theta_{sp1,\bar{R}}) \rangle \cdot \hat{t}_1)$$

$$\cdot (\hat{p}_2^* \cdot \mathbf{F}^*_{\bar{R}_{sp1,\bar{R}} \to \bar{R}_1} \langle \mathbf{R}^*(\theta_{sp1,\bar{R}} \to \bar{R}) \rangle \cdot \hat{t}_2^*) \rangle$$

$$\times \exp [i\kappa_x(x - x_0) + i\kappa_z(z - z_0)] (G - V) * (G - V)$$

$$+ \Gamma^2_{\text{rough}} \langle (\hat{p}_1 \cdot \mathbf{F}_{\bar{R}_{sp1,\bar{R}} \to \bar{R}_1} \langle \mathbf{R}(\theta_{sp1,\bar{R}}) \rangle \cdot \hat{t}_1)$$

$$\cdot (\hat{p}_2^* \cdot \langle \mathbf{R}^*(\theta_{sp1,\bar{R}}) \rangle \mathbf{F}^*_{R_1 \to \bar{R}_{sp1,\bar{R}}} \cdot \hat{t}_2^*) \rangle$$

$$\times \exp [i\kappa_x(x - x_0) - i\kappa_z(z - z_0)] (G - V) * (V - G)$$

$$+ \Gamma^2_{\text{rough}} \langle (\hat{p}_1 \cdot \langle \mathbf{R}(\theta_{sp1,\bar{R}}) \rangle \cdot \mathbf{F}_{\bar{R}_1 \to \bar{R}_{sp1,\bar{R}}} \cdot \hat{t}_1)$$

$$\cdot (\hat{p}_2 \cdot \mathbf{F}^*_{\bar{R}_{sp1,\bar{R}} \to \bar{R}_1} \langle \mathbf{R}^*(\theta_{sp1,\bar{R}}) \rangle \cdot \hat{t}_2) \rangle$$

$$\times \exp [i\kappa_x(x - x_0) + i\kappa_z(z - z_0)] (V - G) * (G - V)$$

$$+ \Gamma^2_{\text{rough}} \langle (\hat{p}_1 \cdot \langle \mathbf{R}(\theta_{sp1,\bar{R}}) \rangle \cdot \mathbf{F}_{\bar{R}_1 \to \bar{R}_{sp1,\bar{R}}} \cdot \hat{t}_1)$$

$$\cdot (\hat{p}_2 \cdot \langle \mathbf{R}^*(\theta_{sp1,\bar{R}}) \rangle \mathbf{F}^*_{\bar{R}_1 \to \bar{R}_{sp1,\bar{R}}} \cdot \hat{t}_2^*) \rangle$$

$$\times \exp [i\kappa_x(x - x_0) - i\kappa_z(z - z_0)] \} (V - G) * (V - G).$$
\hfill (B8)

Inserting (B8) into (4) and noting that the x–y integration is equivalent to the r–η integration results in the cross correlation in (13). Note that for ping-pong mode, in which there is a transmitter at each end of the baseline, the phases of the specular terms in (B4) all become $ik_0(P_1(x, y, z_0) - P_2(x, y, z_0))$ and $\kappa_z \to 0$ in (B8), and the baseline effectively doubles. This is because $\phi_0(z_0) \to 2\phi_0(z_0)$ and κ_x

$\rightarrow 2\kappa_x$. Note that from the single-transmit mode in (14) and the appropriate limits for ping-pong, single-transmit and ping-pong are not simply related by a factor of 2 effective increase in baseline length, as is the case for any of the other models in this paper. The additional decrease in cross-correlation amplitude for the single-transmit case in (14) would be important if the specular return dominated over the volume return, which will probably only be the case for P-band ($\sim$80 cm) and larger wavelengths.

Appendix C: Field Due to a Randomly Oriented Volume and Direct Ground Return

Here we derive the field (19) and cross correlation (20) which leads to the cross correlation (23) due to direct ground returns in the presence of a randomly oriented volume. The fields at the surface must be inserted into (18) to derive the received field (19). The surface field from the direct ground surface return follows from considering the field from small, independent surface patches, of length on a side L. This is equivalent to the Foldy approximation used by *Treuhaft et al.* [1996], in which small elements of the volume are considered to be independent scatterers. The waves scattered from each small patch, due to an incident plane wave propagating in free space, can be expressed in terms of a spatial Fourier series [*Ishimaru*, 1978]. Following *Ishimaru* [1978], (C1) represents a perfectly conducting surface, which is generalized to an arbitrary dielectric constant to arrive at (19). Extending the treatment to account for spherical incident waves propagating through the randomly oriented volume yields the following Fourier series expansions for the field components at the surface location $\vec{R}'(x', y', z')$ from a patch centered at $\vec{R}$ in the x–y plane at $y = 0$ (see Figure C1) for insertion in (18):

$$E_{\hat{t}_1,x}(\vec{R}') = \left. \frac{e^{ik|\vec{R}'-\vec{R}_1|}}{|\vec{R}-\vec{R}_1|} \right|_{z'\partial 0} \exp\left[\frac{2\pi i \rho_0 \langle \hat{t}_1 \cdot \mathbf{F}_f \cdot \hat{t}_1 \rangle h_v}{k_0 \cos \theta_{\vec{R}}} \right]$$
$$\times \sum_{m,n} A_{mn} e^{i(\nu m x' + \nu n y' + b(m,n)z')} \text{ (diffuse only)}$$

$$E_{\hat{t}_1,y}(\vec{R}') = \left[\left. \frac{e^{ik|\vec{R}'-\vec{R}_1|}}{|\vec{R}-\vec{R}_1|} \right|_{z'=0} - \frac{e^{ik\Delta}}{\Delta} \quad \begin{matrix}\text{(incident plus} \\ \text{specular reflection)}\end{matrix} \right.$$
$$+ \left. \left. \frac{e^{ik|\vec{R}'-\vec{R}_1|}}{|\vec{R}-\vec{R}_1|} \right|_{z'=0} \sum_{m,n} B_{mn} e^{i(\nu m x' + \nu n y' + b(m,n)z')} \text{ (diffuse)} \right]$$

Figure C1. A patch of ground surface centered at $\vec{R}$, L on a side, for which the field in equation (19) is calculated. The vector $\vec{R}'$ represents any point within the patch and is the integration variable in equation (18).

$$E_{\hat{t}_1,y}(\vec{R}') = \left[\left. \frac{e^{ik|\vec{R}''-\vec{R}_1|}}{|\vec{R}-\vec{R}_1|} \right|_{z'=0} - \frac{e^{ik\Delta}}{\Delta} \quad \begin{matrix}\text{(incident plus} \\ \text{specular reflection)}\end{matrix} \right.$$
$$+ \left. \left. \frac{e^{ik|\vec{R}''-\vec{R}_1|}}{|\vec{R}-\vec{R}_1|} \right|_{z'=0} \sum_{m,n} B_{mn} e^{i(\nu m x' + \nu n y' + b(m,n)z')} \text{ (diffuse)} \right]$$
$$\cdot \exp\left[\frac{2\pi i \rho_0 \langle \hat{t}_1 \cdot \mathbf{F}_f \cdot \hat{t}_1 \rangle h_v}{k_0 \cos \theta_{\vec{R}}} \right]$$

$$E_{\hat{t}_1,z}(\vec{R}') = \left. \frac{e^{ik|\vec{R}'-\vec{R}_1|}}{|\vec{R}-\vec{R}_1|} \right|_{z'=0} \exp\left[\frac{2\pi i \rho_0 \langle \hat{t}_1 \cdot \mathbf{F}_f \cdot \hat{t}_1 \rangle h_v}{k_0 \cos \theta_{\vec{R}}} \right]$$
$$\times \sum_{m,n} C_{mn} e^{i(\nu m x' + \nu n y' + b(m,n)z')} \text{ (diffuse only)}, \quad \text{(C1)}$$

where the incident field is assumed to be polarized in the $\hat{H}$, or y, direction, and Δ is the total path length for the specular reflection at $\vec{R}_{sp1,\vec{R}'}$, given by

$$\Delta \equiv |\vec{R}' - \vec{R}_{sp1,\vec{R}'}| + |\vec{R}_{sp1,\vec{R}'} - \vec{R}_1|, \quad \text{(C2)}$$

and where, by the wave equation, in the x–z plane,

$$k^2 = (k \sin \theta_{\vec{R}} + \nu m)^2 + (\nu m)^2 + b(m,n)^2. \quad \text{(C3)}$$

In (C1), A_{mn}, B_{mn}, and C_{mn} are the Fourier amplitudes for spatial frequency $m\nu$ and $n\nu$ in the x and y directions, with $\nu = 2\pi/L$. The term $b(m, n)$ is constrained by the wave equation to be

$$b^2(m, n) = k_0^2 - (k_0 \sin\theta_{\bar{R}} + m\nu)^2 - (n\nu)^2. \qquad \text{(C4)}$$

In order to find the surface scattered fields as a function of surface roughness, the surface roughness is expressed as $z' = \zeta(x', y')$ and as a Fourier sum

$$\zeta(x', y') \equiv \sum_{m,n} P(m, n) e^{i\nu m x' + i\nu n y'}$$

with

$$P(m, n) = \frac{1}{L^2} \int_{-L/2}^{L/2} \zeta(x, y) e^{-i[\nu m x + \nu n y]} \, dx \, dy$$

$$\langle P(m, n) P^*(m', n') \rangle = \frac{1}{L^2} \qquad \text{(C5)}$$

$$\cdot \int_{-L/2}^{L/2} \langle \zeta(x, y) \zeta(x_d + x, y_d + y) \rangle e^{-i[\nu m x_d + \nu n y_d]}$$

$$\cdot dx_d \, dy_d \, \delta_{m,m'} \delta_{n,n'} \equiv W(m, n) \delta_{m,m'} \delta_{n,n'}$$

where $x_d \equiv x' - x$ and $y_d \equiv y' - y$. If $k_0\zeta$ is assumed small, then the A_{mn}, B_{mn}, and C_{mn} terms and the exponentials in (C1) can be expanded in terms of $k_0\zeta$ and only first-order terms need to be kept. The tangential boundary conditions on the electric field imply

$$E_{\hat{t}_1, x} + \frac{\partial \zeta}{\partial x'} E_{\hat{t}_1, z} = 0$$

$$\qquad \qquad \qquad \qquad \text{(C6)}$$

$$E_{\hat{t}_1, y} + \frac{\partial \zeta}{\partial y'} E_{\hat{t}_1, z} = 0.$$

Expanding (C1) to first order in $k_0\zeta$, substituting (C1) and (C5) into (C6), and using the divergence Maxwell equation shows

$$A_{mn}^{(1)} = 0$$

$$B_{mn}^{(1)} = 2ik_0 \cos\theta_{\bar{R}} P(m, n)$$

$$C_{mn}^{(1)} = \frac{-2ik_0 \cos\theta_{\bar{R}} \nu n P(m, n)}{b(m, n)}. \qquad \text{(C7)}$$

Substituting the coefficients in (C7) into (C1), using the curl Maxwell equation to find the magnetic field $\bar{\nabla} \times \vec{E}_{\hat{t}_1} = i\omega_0\mu_0\vec{H}_{\hat{t}_1}$, and finally putting (C1) and the

magnetic fields into the surface integral in (18) yields for the field at $\vec{R}_1$, for example, when $\hat{p}_1 = \hat{H} = \hat{t}_1$,

$$\hat{H} \cdot \vec{E}_{\hat{t}_1}(\vec{R}_1, \omega_0; \vec{R})$$

$$= \frac{ik_0}{4\pi} \frac{e^{2ik_0|\vec{R}_1 - \vec{R}|}}{|\vec{R}_1 - \vec{R}|^2} \exp\left[\frac{4\pi i \rho_0 \langle \hat{t}_1 \cdot \mathbf{F}_f \cdot \hat{t}_1 \rangle h_v}{k_0 \cos\theta_{\bar{R}}}\right]$$

$$\times \int dx' \, dy' \sum_{m,n} P(\nu m, \nu n) e^{i((\nu m + 2k_0 \sin\theta_{\bar{R}})x' + \nu n y')}$$

$$\times \left\{ 2ik_0 \cos^2\theta_{\bar{R}} - \frac{2ik_0 \cos\theta_{\bar{R}}}{bk} [\nu^2 n^2 + b^2] \right\}, \qquad \text{(C8)}$$

which generalizes to (19) for arbitrary polarizations and dielectric constants, when the last term in brackets is generalized to $f_{\hat{p}_1, \hat{t}_1}(\nu m, \nu n)$ [Ulaby et al., 1982].

Multiplying (19) by its complex-conjugate analog for reception at $\vec{R}_2$ yields (20), the details of which are below:

$$\langle \hat{p}_1 \cdot \vec{E}_{\hat{t}_1}(\vec{R}_1, \omega_0; \vec{R}) \hat{p}_2^* \cdot \vec{E}_{\hat{t}_2}^*(\vec{R}_2, \omega_0; \vec{R}) \rangle$$

$$= \frac{A^4 k_0^2}{16\pi^2} e^{ik_0|\vec{R}_1 - \vec{R}| - |\vec{R}_2 - \vec{R}|} \exp\left[\frac{+2\sigma_x h_v}{\cos\theta_{\bar{R}}}\right]$$

$$\times \int dx' \, dy' \, dx'' \, dy'' \sum_{m,n,m',n'}$$

$$\cdot \langle P(\nu m, \nu n) P^*(\nu m', \nu n') \rangle e^{i((\nu m + 2k_0 \sin\theta_{\bar{R}})x' + \nu n y')}$$

$$\times e^{-i((\nu m' + 2k_0 \sin\theta_{\bar{R}})x'' + \nu y'')} \langle f_{\hat{p}_1, \hat{t}_1}(\nu m, \nu n) f_{\hat{p}_2, \hat{t}_2}^*(\nu m', \nu n') \rangle$$

$$= \frac{A^4 k_0^2}{16\pi^2} e^{ik_0|\vec{R}_1 - \vec{R}| - |\vec{R}_2 - \vec{R}|}$$

$$\cdot \exp\left[\frac{-2\sigma_x h_v}{\cos\theta_{\bar{R}}}\right] \int dx' \, dy' \, dx'' \, dy''$$

$$\times \sum_{m,n} W(\nu m, \nu n) e^{i((\nu m + 2k_0 \sin\theta_{\bar{R}})(x' - x'') + \nu n(y' - y''))}$$

$$\times \langle f_{\hat{p}_1, \hat{t}_1}(\nu m, \nu n) f_{\hat{p}_2, \hat{t}_2}^*(\nu m, \nu n) \rangle$$

$$\approx \frac{A^4 k_0^2 L^2}{4} e^{ik_0|\vec{R}_1 - \vec{R}| - |\vec{R}_2 - \vec{R}|} \exp\left[\frac{-2\sigma_x h_v}{\cos\theta_{\bar{R}}}\right]$$

$$\times \int d\nu_x \, d\nu_y \, W_P(\nu_x, \nu_y)$$

$$\cdot \langle f_{\hat{p}_1, \hat{t}_1}(\nu_x, \nu_y) f^*_{\hat{p}_2, \hat{t}_2}(\nu_x, \nu_y) \rangle \delta(\nu_x + 2k_0 \sin \theta_{\bar{R}}) \delta(\nu_y)$$

$$= \frac{A^4 k_0^2 L^2}{4} W_P(-2k_0 \sin \theta_{\bar{R}}, 0)$$

$$\times \langle f_{\hat{p}_1, \hat{t}_1}(-2k_0 \sin \theta_{\bar{R}}, 0) f^*_{\hat{p}_2, \hat{t}_2}(-2k_0 \sin \theta_{\bar{R}}, 0) \rangle$$

$$\cdot e^{ik_0 |\vec{R}_1 - \vec{R}| - |\vec{R}_2 - \vec{R}|} \exp\left[\frac{-2\sigma_x h_v}{\cos \theta_{\bar{R}}} \right], \tag{C9}$$

where $\langle P(\nu m, \nu n) P^*(\nu m', \nu n') \rangle \equiv W(\nu m, \nu n) \delta_{m, m'} \delta_{n, n'}$. Noting that as L gets much larger than any characteristic roughness scale, i.e., as the roughness of surface elements becomes uncorrelated, the power spectrum of the roughness at spatial frequencies ν_x, ν_y is given by

$$W_P(\nu_x, \nu_y) \, d\nu_x \, d\nu_y = \lim_{L \to \infty} (L^2/4\pi^2) W(m, n) \Delta \nu_x \Delta \nu_y,$$

with $\Delta \nu_x \equiv 2m\pi/L$ and $\Delta \nu_y \equiv 2n\pi/L$.

Appendix D: Field Due to an Oriented Volume

Here we derive the field (26) which leads to the cross correlation (27) due to an oriented volume. As in Appendix A, the average field at the scatterer at $\vec{R}$ due to a transmitter at $\vec{R}_1$ is needed first. By generalizing the approach used by *Treuhaft et al.* [1996], this field is given by a contribution directly from the transmitter (the first term below) plus one from all other scatterers (the integral):

$$\langle \vec{E}_{\hat{t}_1}(\vec{R}, \omega_0; \vec{R}_1) \rangle = A e^{ik_0 |\vec{R} - \vec{R}_1|} \hat{t}_1$$

$$+ \int \rho_0 \frac{e^{ik_0 |\vec{R}' - \vec{R}|}}{|\vec{R}' - \vec{R}|} \langle \mathbf{F}_{\vec{R}_1 - \vec{R}' \to \vec{R}' - \vec{R}} \rangle \langle \vec{E}_{\hat{t}_1}(\vec{R}', \omega_0; \vec{R}_1) \rangle \, d^3 R',$$
$$\tag{D1}$$

where $\langle \mathbf{F}_{\vec{R}_1 - \vec{R}' \to \vec{R}' - \vec{R}} \rangle$ is the scattering matrix for a wave incident from the transmitter on a volume scatterer at $\vec{R}'$ and scattered toward the scatterer at $\vec{R}$, and $\langle \vec{E}_{\hat{t}_1}(\vec{R}', \omega_0; \vec{R}_1) \rangle$ is the average field at the scatterer at $\vec{R}'$. All other terms are defined after (5) in the text. If the average scattering matrix is a multiple of the identity matrix, as it is for a randomly oriented volume, then all terms in (D1) are in the $\hat{t}_1$ direction and (D1) becomes a scalar integral equation for the field incident on $\vec{R}$ with a solution which eventually leads to the backscattered field in (5). If the volume is oriented, then the action of

$\langle \mathbf{F}_{\vec{R}_1 - \vec{R}' \to \vec{R}' - \vec{R}} \rangle$ on $\langle \vec{E}_{\hat{t}_1}(\vec{R}', \omega_0; \vec{R}_1) \rangle$ will introduce components in (D1) which are orthogonal to $\hat{t}_1$, and (D1) becomes a vector integral equation. Because the method of stationary phase [*Ishimaru*, 1978] shows that only the average forward scattering matrix $\langle \mathbf{F}_f \rangle$ enters into the solution of (D1), expanding all field components in terms of the eigenvectors of $\langle \mathbf{F}_f \rangle$, $\hat{p}_a$ and $\hat{p}_b$, assumed orthogonal (i.e., $\langle \mathbf{F}_f \rangle$ is symmetric) yields

$$(\langle \vec{E}_{\hat{t}_1}(\vec{R}, \omega_0; \vec{R}_1) \rangle \cdot \hat{p}_a) \hat{p}_a + (\langle \vec{E}_{\hat{t}_1}(\vec{R}, \omega_0; \vec{R}_1) \rangle \cdot \hat{p}_b) \hat{p}_b$$

$$= A e^{ik_0 |\vec{R} - \vec{R}_1|} (\hat{t}_1 \cdot \hat{p}_a) \hat{p}_a + \int \rho_0 \frac{e^{ik_0 |\vec{R}' - \vec{R}|}}{|\vec{R}' - \vec{R}|} (\langle \mathbf{F}_f \rangle \hat{p}_a)$$

$$\cdot \langle \vec{E}_{\hat{t}_1}(\vec{R}', \omega_0; \vec{R}_1) \rangle \cdot \hat{p}_a \, d^3 R' + A e^{ik_0 |\vec{R} - \vec{R}_1|} (\hat{t}_1 \cdot \hat{p}_b) \hat{p}_b$$

$$+ \int \rho_0 \frac{e^{ik_0 |\vec{R}' - \vec{R}|}}{|\vec{R}' - \vec{R}|} (\langle \mathbf{F}_f \rangle \hat{p}_b) \langle \vec{E}_{\hat{t}_1}(\vec{R}', \omega_0; \vec{R}_1) \rangle \cdot \hat{p}_b \, d^3 R'.$$
$$\tag{D2}$$

As is suggested by (D2), separating the terms involving $\hat{p}_a$ from those involving $\hat{p}_b$ results in two integral equations equivalent to the case in which $\langle \mathbf{F}_f \rangle$ is the identity matrix. The method of stationary phase yields the solution for each of the $\hat{p}_a$ and $\hat{p}_b$ components, and their sum forms for the total average field incident at $\vec{R}$:

$$\langle \vec{E}_{\hat{t}_1}(\vec{R}, \omega_0; \vec{R}_1) \rangle = A(\hat{t}_1 \cdot \hat{p}_a) \hat{p}_a$$

$$\cdot \exp\left[ik_0 |\vec{R} - \vec{R}_1| + \frac{2\pi i \rho_0 \lambda_a (h_v - z)}{k_0 \cos \theta_{\bar{R}}} \right] + A(\hat{t}_1 \cdot \hat{p}_b) \hat{p}_b$$

$$\cdot \exp\left[ik_0 |\vec{R} - \vec{R}_1| + \frac{2\pi i \rho_0 \lambda_b (h_v - z)}{k_0 \cos \theta_{\bar{R}}} \right], \tag{D3}$$

where λ_a and λ_b are the complex eigenvalues of $\langle \mathbf{F}_f \rangle$. From the definition of refractivity and extinction, the eigenvalues are

$$\frac{2\pi \rho_0}{k_0} \lambda_i = k_0 \chi_i + i \frac{\sigma_{x_i}}{2}, \tag{D4}$$

where i takes on the index a and b and χ_i and σ_{x_i} are the refractivity and extinction coefficient, respectively, for eigenpolarization $\hat{p}_i$. Note that if σ_{x_a} is different from σ_{x_b}, a wave incident at an arbitrary polarization will change its polarization as it propagates into the volume. However, at either $\hat{p}_a$ or $\hat{p}_b$, the wave will retain its polarization, but each will propagate with different characteristics, as is schematically indicated by Figure 5c.

In order to calculate the field received at $\vec{R}_1$ (equation (26)), (D3) must be operated on by the backscattering matrix $\mathbf{F}_b$ and a free-space propagator (the first term below) and propagated back through the rest of the volume (the integral):

$$\vec{E}_{\hat{t}_1}(\vec{R}_1, \omega_0; \vec{R}) = A \frac{e^{ik_0|\vec{R}_1 - \vec{R}|}}{|\vec{R}_1 - \vec{R}|} \mathbf{F}_b \langle \vec{E}_{\hat{t}_1}(\vec{R}, \omega_0; \vec{R}_1) \rangle$$

$$+ \int \rho_0 \frac{e^{ik_0|\vec{R}_1 - \vec{R}'|}}{|\vec{R}_1 - \vec{R}'|} \langle \mathbf{F}_f \rangle \langle \vec{E}_{\hat{t}_1}(\vec{R}', \omega_0; \vec{R}) \rangle \, d^3 R'$$

$$\approx A^2 e^{2ik_0|\vec{R}_1 - \vec{R}|} \mathbf{F}_b \sum_i (\hat{t}_1 \cdot \hat{p}_i) \hat{p}_i$$

$$\cdot \exp \left[\frac{ik_0 \chi_i (h_v - z)}{\cos \theta_{\vec{R}}} - \frac{\sigma_{x_i}(h_v - z)}{2 \cos \theta_{\vec{R}}} \right]$$

$$+ \int \rho_0 \frac{e^{ik_0|\vec{R}_1 - \vec{R}'|}}{|\vec{R}_1 - \vec{R}'|} \langle \mathbf{F}_f \rangle \sum_j (\hat{p}_j \cdot \langle \vec{E}_{\hat{t}_1}(\vec{R}', \omega_0; \vec{R}) \rangle) \hat{p}_j$$

$$\cdot d^3 R' = A^2 e^{2ik_0|\vec{R}_1 - \vec{R}|} \sum_j \hat{p}_j \sum_i (\hat{t}_1 \cdot \hat{p}_i)$$

$$\cdot (\hat{p}_j \cdot \mathbf{F}_b \cdot \hat{p}_i) \exp \left[\frac{ik_0 \chi_i (h_v - z)}{\cos \theta_{\vec{R}}} - \frac{\sigma_{x_i}(h_v - z)}{2 \cos \theta_{\vec{R}}} \right]$$

$$+ \int \rho_0 \frac{e^{ik_0|\vec{R}_1 - \vec{R}'|}}{|\vec{R}_1 - \vec{R}'|} \sum_j \lambda_j (\hat{p}_j \cdot \langle \vec{E}_{\hat{t}_1}(\vec{R}', \omega_0; \vec{R}) \rangle) \hat{p}_j \, d^3 R'.$$
$$(D5)$$

Comparing (D5) with (D2) yields a solution for the field at $\vec{R}_1$ analogous to (D3):

$$\vec{E}_{\hat{t}_1}(\vec{R}_1, \omega_0; \vec{R}) = A^2 e^{2ik_0|\vec{R}_1 - \vec{R}|}$$

$$\cdot \sum_j \hat{p}_j \exp \left[\frac{ik_0 \chi_j (h_v - z)}{\cos \theta_{\vec{R}}} - \frac{\sigma_{x_j}(h_v - z)}{2 \cos \theta_{\vec{R}}} \right]$$

$$\times \sum_i (\hat{t}_1 \cdot \hat{p}_i)(\hat{p}_j \cdot \mathbf{F}_b \cdot \hat{p}_i)$$

$$\cdot \exp \left[\frac{ik_0 \chi_i (h_v - z)}{\cos \theta_{\vec{R}}} - \frac{\sigma_{x_i}(h_v - z)}{2 \cos \theta_{\vec{R}}} \right] = A^2 e^{2ik_0|\vec{R}_1 - \vec{R}|}$$

$$\times \sum_{i,j} \hat{p}_j (\hat{t}_1 \cdot \hat{p}_i)(\hat{p}_j \cdot \mathbf{F}_b \cdot \hat{p}_i)$$

$$\cdot \exp \left[\frac{ik_0 (\chi_i + \chi_j)(h_v - z)}{\cos \theta_{\vec{R}}} - \frac{(\sigma_{x_i} + \sigma_{x_j})(h_v - z)}{2 \cos \theta_{\vec{R}}} \right].$$
$$(D6)$$

Taking the inner product of (D6) with the receive polarization $\hat{p}_1$ yields the field received at $\vec{R}_1$ due to an oriented volume (26).

References

Asner, G. P., C. A. Wessman, and D. S. Schimel, Heterogeneity of savanna canopy structure and function from imaging spectrometry and inverse modeling, *Ecol. Appl.*, *8*, 926–941, 1998.

Beckmann, P., and A. Spizzichino, *The Scattering of Electromagnetic Waves From Rough Surfaces*, p. 81, Pergamon, Tarrytown, N. Y., 1963.

Cloude, S. R., An entropy based classification scheme for land applications of polarimetric SAR, *IEEE Trans. Geosci. Remote Sens.*, *35*, 68–78, 1997.

Cloude, S. R., and K. P. Papathanassiou, Polarimetric SAR interferometry, *IEEE Trans. Geosci. Remote Sens.*, *36*, 1551–1565, 1998.

Cloude, S. R., and E. Pottier, A review of target decomposition theorems in radar polarimetry, *IEEE Trans. Geosci. Remote Sens.*, *34*, 498–518, 1996.

Durden, S. L., J. J. van Zyl, and H. A. Zebker, Modeling and observation of the radar polarization signature of forested areas, *IEEE Trans. Geosci. Remote Sens.*, *27*, 290–301, 1989.

Franklin, J. F., and T. A. Spies, Ecological definitions of old-growth Douglas-fir forests, in *Wildlife and Vegetation of Unmanaged Douglas-Fir Forests*, edited by L. Ruggiero, pp. 61–69, *Gen. Tech. Rep. PNW-GTR-285*, U.S. Dep. of Agric. Pac. Northwest Res. Stn., Portland, Oreg., 1991.

Freeman, A., and S. L. Durden, A three-component scattering model for polarimetric SAR data, *IEEE Trans. Geosci. Remote Sens.*, *36*, 963–973, 1998.

Hagberg, J. O., L. M. H. Ulander, and J. Askne, Repeat-

pass SAR interferometry over forested terrain, *IEEE Trans. Geosci. Remote Sens.*, *33*, 331–340, 1995.

Hamilton, W. C., *Statistics in Physical Science: Estimation, Hypothesis Testing, and Least Squares*, Ronald Press, New York, 1964.

Ishimaru, A., *Wave Propagation and Scattering in Random Media*, vol. 2, pp. 474–475, Academic, San Diego, Calif., 1978.

Jackson, J. D., *Classical Electrodynamics*, p. 432, John Wiley, New York, 1975.

Lang, R. H., Electromagnetic backscattering from a sparse distribution of lossy dielectric scatterers, *Radio Sci.*, *16*, 15–30, 1981.

Lax, M., Multiple scattering of waves, *Rev. Mod. Phys.*, *23*, 287–310, 1951.

Lin, Y. C., and K. Sarabandi, Retrieval of forest parameters using a fractal-based coherent scattering model and a genetic algorithm, *IEEE Trans. Geosci. Remote Sens.*, part 1, *37*, 1415–1424, 1999.

Means, J. E., S. A. Acker, D. J. Harding, J. B. Blair, M. A. Lefsky, W. B. Cohen, M. E. Harmon, and W. A. McKee, Use of large-footprint scanning airborne lidar to estimate forest stand characteristics in the western Cascades of Oregon, *Remote Sens. Environ.*, *67*, 298–308, 1999.

Moghaddam, M., Effect of medium symmetries on parameter estimation with polarimetric interferometry, *J. Electromagn. Waves Appl.*, *14*, 173–184, 2000.

Moghaddam, M., and S. S. Saatchi, Analysis of scattering mechanisms in SAR imagery over boreal forest—Results from BOREAS-93, *IEEE Trans. Geosci. Remote Sens.*, *33*, 1290–1296, 1995.

Mooney, H. A., and R. J. Hobbs, Remote sensing of biosphere function, in *Ecological Studies*, vol. 79, edited by R. J. Hobbs and H. A. Mooney, pp. 1–4, Springer-Verlag, New York, 1990.

Neilson, R. P., A model for predicting continental-scale vegetation distribution and water balance, *Ecol. Appl.*, *5*, 362–385, 1995.

Nghiem, S. V., S. H. Yueh, R. Kwok, and F. K. Li, Symmetry properties in polarimetric remote sensing, *Radio Sci.*, *27*, 693–711, 1992.

Sarabandi, K., Delta-K-radar equivalent of interferometric SARS—A theoretical study for determination of vegetation height, *IEEE Trans. Geosci. Remote Sens.*, *35*, 1267–1276, 1997.

Schuler, D. L., T. L. Ainsworth, and G. Degrandi, Topographic mapping using polarimetric SAR data, *Int. J. Remote Sens.*, *19*, 141–160, 1998.

Thompson, T., J. van Zyl, S. Hensley, K. Wheeler, R. Bartman, J. Reis, R. Munjy, J. Burton, and R. Yoha, GeoSAR: A new radar terrain mapping system for the new millenium, paper presented at the XXVI General Assembly of the International Union of Radio Science, Toronto, Canada, Aug. 1999.

Treuhaft, R. N., and S. R. Cloude, The structure of oriented vegetation from polarimetric interferometry, *IEEE Trans. Geosci. Remote Sens.*, *37*, 2620–2624, 1999.

Treuhaft, R. N., S. N. Madsen, M. Moghaddam, and J. J. van Zyl, Vegetation characteristics and surface topography from interferometric radar, *Radio Sci.*, *31*, 1449–1485, 1996.

Treuhaft, R. N., M. Moghaddam, and B. J. Yoder, Forest vertical structure from multibaseline interferometric radar for studying growth and productivity, in *Remote Sensing: A Scientific Vision for Sustainable Development*, pp. H6–06, IEEE Press, Piscataway, N. J., 1997.

Tsang, L., J. A. Kong, and R. T. Shin, *Theory of Microwave Remote Sensing*, John Wiley, New York, 1985.

Ulaby, F. T., R. K. Moore, and A. K. Fung, *Microwave Remote Sensing, Active and Passive*, vol. II, Artech House, Norwood, Mass., 1982.

Valenzuela, G. R., Depolarization of EM waves by slightly rough surfaces, *IEEE Trans. Antennas Propag.*, *15*, 552–557, 1967.

Waring, R. H., J. Way, R. Hunt Jr., L. Morrissey, K. J. Ranson, J. F. Weishampel, R. Oren, and S. E. Franklin, Imaging radar for ecosystem studies, *BioScience*, *45*, 715–723, 1995.

Wegmuller, U., and C. Werner, Retrieval of vegetation parameters with SAR interferometry, *IEEE Trans. Geosci. Remote Sens.*, *35*, 18–24, 1997.

Zebker, H. A., S. N. Madsen, J. Martin, K. B. Wheeler, T. Miller, Y. Lou, G. Alberti, S. Vetrella, and A. Cucci, The TOPSAR interferometric radar topographic mapping instrument, *IEEE Trans. Geosci. Remote Sens.*, *30*, 933–940, 1992.

———————

P. R. Siqueira and R. N. Treuhaft, Jet Propulsion Laboratory, California Institute of Technology, 4800 Oak Grove Drive, MS 138-212, Pasadena, CA 91109-8099. (rnt@radar-sci.jpl.nasa.gov)